Data-Driven Inference of the Mechanics of Slip Along Glacier Beds Using Physics-Informed Neural Networks

Bryan Riel
Department of Earth, Atmospheric and Planetary Sciences
Massachusetts Institute of Technology
Cambridge, MA 02139
`briel@mit.edu`

Brent Minchew
Department of Earth, Atmospheric and Planetary Sciences
Massachusetts Institute of Technology
Cambridge, MA 02139
`minchew@mit.edu`

Tobias Bischoff
Climate Modeling Alliance
California Insitute of Technology
Pasadena, CA 91125
`tobias@caltech.edu`

This manuscript is a non-peer reviewed EarthArXiv preprint that has been submitted for publication in *Science Advances*.

Abstract

Reliable projections of sea-level rise depend on accurate representations of how fast-flowing glaciers slip along their beds. The mechanics of slip are often parameterized as a constitutive relation (or ‘sliding law’) whose proper form remains uncertain. Here, we present a novel deep learning-based framework for learning the time evolution of drag at glacier beds from time-dependent ice velocity and elevation observations. We use a stochastic neural network, informed by the governing equations of ice flow, to infer spatially and temporally varying basal drag and associated uncertainties from data. We test the framework on 1D and 2D ice flow simulation outputs and demonstrate the recovery of the underlying basal mechanics under various levels of observational and modeling uncertainties. We apply this framework to time-dependent velocity data for Rutford Ice Stream, Antarctica, and present evidence that ocean-tide-driven changes in subglacial water pressure drive changes in ice flow over the tidal cycle.

1 Introduction

Fast-flowing outlet glaciers that drain the Greenland and Antarctic Ice Sheets are major contributors to sea-level rise (SLR) [9, 66]. While widespread acceleration of these glaciers in response to changing climate conditions has magnified their importance in future projections of SLR, fundamental uncertainties about their long-term dynamical behavior and stability persist [67]. One of the key sources of uncertainty is the unknown form of the parameterization used to describe how drag at the base of glaciers is related to basal sliding velocity, bed roughness, bed composition, and water pressure [66, 2]. The resistive force provided by basal drag plays a significant role in the evolution of glaciers in response to changes in atmospheric and oceanic conditions. The collection of proposed parameterizations for basal drag are commonly referred to as sliding laws, and the wide range of physical processes governing the interaction between ice, bed materials, and basal hydrology have led to a wide spectrum of proposed sliding laws for quantifying drag dependence on sliding velocity.

Despite considerable advances in our understanding of the mechanics of slip along glacier beds, no consensus has emerged as to which sliding law offers the best balance of model simplicity and model fidelity, though one model has emerged as a candidate for a universal sliding law that is applicable to glaciers with rigid and deforming beds [72, 32, 85]. Since the physical processes meant to be represented by the sliding law are not directly observable outside of laboratory settings, inference of the form of the the sliding law and the value of its parameters requires inverse modeling using observations of ice surface velocity and elevation coupled with an accurate physical model of ice flow [34, 75, 17, 8].

Fortunately, the Earth science community has seen a sharp rise in remote sensing data availability over the past two decades. This rise is due to an ever-increasing number of spaceborne and airborne Earth-observing platforms in combination with increased computational capabilities and data-providing services that operationally produce analysis-ready data sets. The glaciology community has benefited enormously from continent-wide observations of ice surface velocities and elevation over much of the Greenland and Antarctic Ice Sheets [65, 31, 56, 28]. However, within the context of modeling of basal drag, use of these observations in modeling efforts have traditionally involved assimilating instantaneous or time-averaged velocity observations into ice flow models in order to estimate static distributions of basal drag [42, 51, 39, 75]. A few studies have expanded upon this approach by estimating basal drag at different time epochs, which can be used to attribute changes in drag to known changes in environmental factors like surface meltwater [47] or to better constrain parameters in sliding laws [23, 17]. The increasing availability of time-dependent velocity fields, which in many places capture the evolution of glacier velocities on sub-monthly timescales in high-spatial resolution, could potentially provide much finer resolution on the time-evolution of basal drag in order to obtain the underlying space- and time-varying functional form of the sliding law.

Within the past decade, machine learning algorithms have exploded in popularity due to their ability to discover patterns and relationships in large volumes of data which are used to inform numerous predictive and analytical tasks [40]. In particular, the recent success of deep learning has been attributed to the ability to learn hierarchical, abstract features in unstructured data which can interact in highly non-linear ways [5]. The coincident increase in computing power, in large part from the increased utility of graphics processing units, has led to rapid development of specialized network architectures able to learn patterns from video streams, images, and word sequences. Recently, many studies have demonstrated the potential for deep learning algorithms to be integrated with scientific knowledge in order to bridge theoretic gaps, discover new and robust patterns in scientific observations, and predict the evolution of dynamical systems [35, 58, 62]. This type of "theory-guided" learning combines the robustness provided by decades of theoretical and experimental work with the pattern recognition and representation power of deep learning.

In this work, we develop a hybrid modeling framework that can exploit contemporary remote sensing data by incorporating well-known ice dynamics and constitutive laws with a deep neural network model representing the unknown sliding law. In developing this framework, our goal is to demonstrate a general approach for inferring various components of a glacier system from large volumes of data without requiring access to sophisticated ice flow models. We further discuss how we can pose the learning problem in a probabilistic manner that partially allows for the quantification of uncertainties due to both data errors and uncertainties in the governing equations of ice flow. Since the focus of this work is on learning a spatiotemporal representation for basal drag, we apply our method to several one- and two-dimensional flowline simulations that are representative of real-world basal sliding scenarios that would be challenging to analyze with traditional inverse modeling approaches. Finally, we apply our methods to real velocity data over Rutford Ice Stream in West Antarctica and present observational evidence for the role of subglacial hydrology in propagating tidally driven variations in ice flow roughly 100 km inland.

2 Results

2.1 Ice Flow Governing Equations

The flow of ice is well-approximated by incompressible Stokes flow, which describes the motion of a viscous fluid where inertial forces are negligibly small relative to viscous forces. In Stokes flow, the momentum equations (stress balance) reduce to gravitational body forces resisted by stresses induced through ice deformation and shear stresses at the interfaces between ice and the bed and sidewalls. For many fast-flowing outlet glaciers and ice streams, flow is dominated by basal sliding where sliding velocity is comparable to surface velocity, and forward motion due to vertical shearing is negligible. In this case, the full three-dimensional Stokes equations can be reduced by neglecting certain components of the stress divergence and averaging the resulting momentum balance over depth (see Materials and Methods). This approximation, commonly referred to as the Shallow Ice Shelf/Stream Approximation (SSA), leads to the following two-dimensional relation in a Cartesian coordinate system with z defined parallel to the gravity vector:

$$\frac{\partial}{\partial x}\left(2\eta h\left(2\frac{\partial u}{\partial x}+\frac{\partial v}{\partial y}\right)\right)+\frac{\partial}{\partial y}\left(\eta h\left(\frac{\partial u}{\partial y}+\frac{\partial v}{\partial x}\right)\right)-\tau_{bx}=\rho_i g h\frac{\partial s}{\partial x}, \tag{1a}$$

$$\frac{\partial}{\partial y}\left(2\eta h\left(2\frac{\partial v}{\partial y}+\frac{\partial u}{\partial x}\right)\right)+\frac{\partial}{\partial x}\left(\eta h\left(\frac{\partial u}{\partial y}+\frac{\partial v}{\partial x}\right)\right)-\tau_{by}=\rho_i g h\frac{\partial s}{\partial y}, \tag{1b}$$

where u and v are the horizontal velocity components of the velocity vector, $\mathbf{u}$, along the x- and y-directions, respectively, and taken to be constant with depth; h is the ice thickness; τ_{bx} and τ_{by} represent the x- and y-components of basal drag; s is the ice surface elevation; η is the effective dynamic viscosity; ρ_i is the mass density of ice; and g is the gravitational acceleration. Basal drag is modeled with a sliding law using a power-law relationship [83]:

$$\tau_{bx}=c_b\|\mathbf{u}\|^{\frac{1}{m}}\frac{u}{\|\mathbf{u}\|}, \tag{2a}$$

$$\tau_{by}=c_b\|\mathbf{u}\|^{\frac{1}{m}}\frac{v}{\|\mathbf{u}\|}, \tag{2b}$$

where $\|\mathbf{u}\|=\sqrt{u^2+v^2}$, c_b acts as a drag coefficient, and m is a scalar. Thus, the basal drag magnitude is a (potentially nonlinear) function of the surface velocity, which is assumed to be approximately equal to the basal velocity. The range of possible values for m is wide and determines whether sliding at the bed is rate-weakening ($m<0$, basal drag decreases with sliding velocity), rate-strengthening ($m>0$, basal drag increases with sliding velocity), or rate-independent ($m\to\infty$). The mode of sliding can have strong implications on how stress perturbations at the termini of glaciers propagate upstream [22]. Recent laboratory work [85] has shown that these sliding modes can be represented as a spectrum of sliding behavior corresponding to rate-strengthening sliding over rigid beds at velocities below a certain threshold, above which till deformation dominates and basal drag is largely rate-independent.

In this work, we simulate and analyze ice flow in both 1D and 2D in order to demonstrate our proposed learning framework on systems of increasing complexity. For both classes of simulations, we model tidewater glaciers where their termini end at the ocean but are grounded throughout the entire modeling domain. In 1D, the particular model form we use in this work reduces the 2D momentum balance equations (Equations 1a,b) by assuming that lateral shear stresses are negligible, which is appropriate for ice streams that are much wider than they are thick [74]. Thus, Equations 1a,b reduce to:

$$2\frac{\partial}{\partial x}\left[h\eta\frac{\partial u}{\partial x}\right]-\tau_b=\rho_i g h\frac{\partial s}{\partial x}, \tag{3}$$

with x defined as parallel to flow. We induce velocity variations by periodically varying the longitudinal stress conditions at the terminus, which approximates the periodic rising and falling of ocean levels due to tides (see Materials and Methods). Thus, the final simulation outputs we use as inputs and data for the machine learning models are the time-dependent velocity components and ice thickness.

We use a basal drag sliding relationship where the prefactor c_b can vary in both space and time and the exponent m can vary in space such that:

$$\tau_b\left(x,t\right)=c_b\left(x,t\right)|u|^{1/m(x)}. \tag{4}$$

The spatial variation of c_b and m can represent changes in bed roughness and composition, ice cavity density, and basal water pressure, among other factors. The temporal variation of c_b can represent local changes in basal water pressure due to an evolving subglacial hydrological system, which has been shown to be an important process in many fast-flowing tidewater glaciers around the globe [73, 26]. It is not possible to recover estimates of c_b and m using traditional inverse modeling techniques with velocity observations at a single epoch due to the non-uniqueness of these parameters for a given value of basal drag, τ_b. Therefore, simulations generated with these types of variations are both realistic and useful for demonstrating the utility of time-dependent velocity and elevation fields for inferring basal mechanics.

2.2 Neural Network Representation of Basal Drag

Large uncertainties on the form of the sliding law motivate a more flexible representation of basal drag as a function of sliding velocity, as well as a function of space and time in the case of spatially-varying till properties or subglacial hydrology. To that end, let us consider the following:

$$\hat{\tau}_b = f_{\boldsymbol{\theta}}\left(u, x, t\right), \tag{5}$$

where basal drag predictions $\hat{\tau}_b$ are generated by a generic nonlinear function of sliding velocity, spatial coordinate, and time. The nonlinear function is itself represented by a feedforward neural network parameterized by $\boldsymbol{\theta}$, the weights and biases of the hidden layers. The utility of multi-layer neural networks as universal function approximators (for sufficient layer widths, depth, and non-linear activation functions) makes them well suited to represent an approximation to the τ_b function [7]. We emphasize that in the general case, any neural network representation for a given function is a "black-box" and not immediately interpretable. However, for the case of glacier mechanics, the ability to evaluate the basal drag model for any combination of sliding velocity and space and time coordinate permits subsequent interpretation of the nonlinear model and possible inference of the underlying functional form.

2.2.1 Learning Basal Drag Function with Hybrid Modeling

Basal drag is not directly observable. To learn the functional approximation, we must combine quantities that are readily observable (e.g., ice velocity and surface elevation) within the physical modeling framework provided by the momentum balance equations (Equations 1a,b). The data distribution for direct observables are thus transformed into a distribution of pseudo-observables, which is then used to train the neural network. As an illustration, let us consider the cost function for the learning objective for the 1D shallow ice stream case (Equation 3):

$$\mathcal{L}_{pde}\left(\boldsymbol{\theta}\right) = \frac{1}{Q}\sum_{k=1}^{Q}\left(f_{\boldsymbol{\theta}}^{k} - \tilde{\tau}_b^{k}\right)^2, \tag{6}$$

where we use the notation $f_{\boldsymbol{\theta}}^{k} = f_{\boldsymbol{\theta}}\left(u^k, x^k, t^k\right)$ and $\tilde{\tau}_b^k = \tilde{\tau}_b\left(u^k, h^k, x^k, t^k\right)$ for brevity. The variable $\tilde{\tau}_b$ represents the "expected" basal drag as computed from the momentum balance, which for the 1D case (Equation 3) is:

$$\tilde{\tau}_b = 2\frac{\partial}{\partial x}\left(h\eta\frac{\partial u}{\partial x}\right) - \rho_i g h \frac{\partial s}{\partial x}. \tag{7}$$

Equation 7 can be extended to 2D or 3D to include lateral and vertical shear stress effects. The cost function (Equation 6) is thus a mean square error (MSE) over Q examples between the drag neural network predictions and the expected basal drag.

We can supplement Equation 6 with additional known physical constraints encapsulated in a separate loss function $\mathcal{L}_{ph}\left(\boldsymbol{\theta}\right)$. For example, we may wish to enforce that drag can only resist flow (never drive flow) so that drag is negative by the convention in Equation 7. Additionally, we may wish to encourage spatially smooth drag predictions since the viscous nature of ice flow nominally damps out basal drag variations at smaller wavelengths [24]. These two constraints can be implemented as:

$$\mathcal{L}_{ph}\left(\boldsymbol{\theta}\right) = \frac{1}{P}\sum_{k=1}^{P}\left[\mathrm{ReLU}\left(f_{\boldsymbol{\theta}}^{k}\right) + \left(\left(\frac{\partial^2 f_{\boldsymbol{\theta}}^{k}}{\partial x^{k^2}}\right)^2 + \left(\frac{\partial^2 f_{\boldsymbol{\theta}}^{k}}{\partial y^{k^2}}\right)^2\right)\right], \tag{8}$$

where the rectified linear unit (ReLU) function is zero for negative values and identity for positive values, and the second term implements Laplacian smoothing. The first constraint may also be implemented by applying a negative ReLU activation on the outputs of $f_{\boldsymbol{\theta}}$. Note that the number of examples P for $\mathcal{L}_{ph}\left(\boldsymbol{\theta}\right)$ is not necessarily equal to the number of examples Q used for $\mathcal{L}_{pde}\left(\boldsymbol{\theta}\right)$. For the latter, the Q examples are dictated by the availability of velocity and ice thickness gradients, whereas the P examples for the former can be evaluated anywhere within the training domain.

For all formulations of the longitudinal stress gradients and any additional gradient-based penalties, first- and second-order spatial derivatives of velocity and elevation are required. These gradients may be computed *a priori* from the velocity and elevation measurements and used to train $f_{\boldsymbol{\theta}}$ directly. However, the highly-nonlinear form of the non-Newtonian effective ice viscosity (see Materials and Methods) can result in large amplification of the gradients and any errors associated with them. The gradients themselves may be difficult to compute when data are missing or are scattered in space. We approach these challenges by modeling the velocity and elevation observations themselves with another neural network, such that:

$$\hat{\mathbf{d}} = g_{\boldsymbol{\phi}}\left(x, t\right), \tag{9}$$

where the network weights are parameterized by $\boldsymbol{\phi}$. In addition to velocity predictions, $\hat{u}$, the prediction vector $\hat{\mathbf{d}}$ can contain either surface elevation or thickness predictions which are interchangeable when knowledge of the bed is assumed to be error-free. In the general case where the bed is known to have non-negligible uncertainties, $\hat{\mathbf{d}}$ may include velocity, elevation, and thickness. For the purpose of this discussion, we assume $\hat{\mathbf{d}} = [\hat{u}, \hat{h}]$ where $\hat{h}$ is the predicted thickness.

The loss function for $g_{\boldsymbol{\phi}}$ is a standard MSE between predictions and observations, $\mathbf{d} = [u, h]$:

$$\mathcal{L}_{mse}\left(\boldsymbol{\phi}\right) = \frac{1}{M}\sum_{k=1}^{M}\left[(u^k - \hat{u}^k)^2 + (h^k - \hat{h}^k)^2\right], \tag{10}$$

where $g^k_{\boldsymbol{\phi}} = g_{\boldsymbol{\phi}}\left(x^k, t^k\right)$, and M data points are used for training $g_{\boldsymbol{\phi}}$. The key advantage of the neural network representation $g_{\boldsymbol{\phi}}$ is the ability to evaluate derivatives of u and h at arbitrary space and time coordinates at machine precision using automatic differentiation [4, 58]. Essentially, the neural network learns a smooth hypersurface between scattered observations in data space and can return the hypersurface value and slope at any given point. Of course, the smoothness of this surface will depend on the network capacity (i.e., layer size and depth), as well as the activation function used between layers (see Appendix B for network and training details). These smoothed predictions and their gradients are then used to generate the inputs and expected basal drag for training $f_{\boldsymbol{\theta}}$. Thus, we use $\hat{u}$ and $\hat{h}$ rather than u and h to compute the losses $\mathcal{L}_{pde}$ and $\mathcal{L}_{ph}$ (Figure 1).

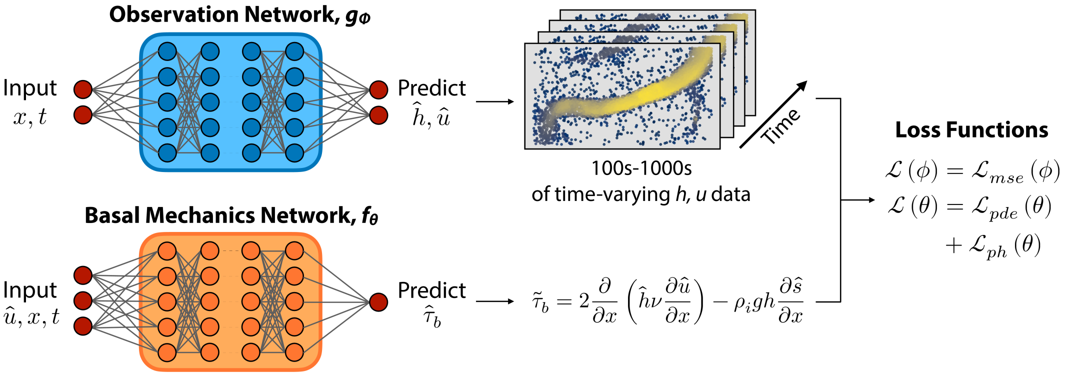

Figure 1: Diagram of neural network architecture and learning process. Scattered spatial and time coordinates are input into network $g_{\boldsymbol{\phi}}$, which is trained to generate predictions of ice surface velocity and thickness, $\hat{u}$ and $\hat{h}$, at those coordinates. Velocity and thickness predictions and space and time coordinates (which may differ from coordinates input to $g_{\boldsymbol{\phi}}$) are input into a second network, $f_{\boldsymbol{\theta}}$, which is trained to predict basal drag estimated from ice flow momentum balance equations (1D momentum balance used here as an example). A combined loss function is then used to train the neural network weights, $\boldsymbol{\phi}$ and $\boldsymbol{\theta}$, simultaneously.

To train $f_{\boldsymbol{\theta}}$ and $g_{\boldsymbol{\phi}}$ simultaneously, we formulate the joint learning objective:

$$\boldsymbol{\theta}, \boldsymbol{\phi} = \underset{\boldsymbol{\theta}, \boldsymbol{\phi}}{\arg\min}\left[\mathcal{L}_{mse}\left(\boldsymbol{\phi}\right) + \lambda\mathcal{L}_{pde}\left(\boldsymbol{\theta}\right) + \alpha\mathcal{L}_{ph}\left(\boldsymbol{\theta}\right)\right], \tag{11}$$

where the hyperparameters λ and α control the relative strengths of the partial differential equation (PDE) consistency and additional physical constraint loss functions, respectively. The choice of

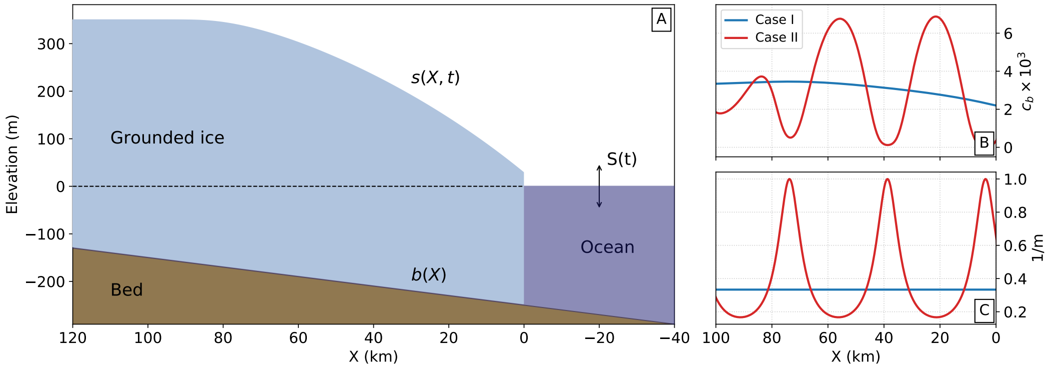

Figure 2: Experimental setup and initial ice geometry for 1D simulations of a marine-terminating glacier. A) Initial grounded ice (light blue) slides on its bed (dark brown) below sea level (dark blue; dashed black line). For perturbation experiments, ocean level $S(t)$ is periodic in time. X-coordinates indicate distance upstream from terminus. The ice surface, $s(X,t)$, varies in space and time while the bed, $b(X)$, varies only in space. Spatial distributions of prefactor values, c_b (B) and exponents, $1/m$ (C) for two different simulation scenarios with different sliding modes but similar levels of basal stress. Case I (blue lines) corresponds to a constant exponent and slowly-varying prefactor while Case II (red lines) corresponds to periodically varying exponent and prefactor profiles. The values for Case II are chosen such that the steady-state basal drag values are roughly equal to the steady-state drag for Case I.

these parameters will generally be controlled by data quality (noise level, spatiotemporal coverage, accuracy of bed topography, etc.) and *a priori* uncertainties on the parameterization of ice flow (e.g., rheology, spatial smoothness of drag, etc.) and can be computed using standard model selection techniques like cross-validation or using an L-curve (Figure S5). A key point to reiterate is that for the above learning objective, observed data are only used for the cost function $\mathcal{L}_{mse}\left(\boldsymbol{\phi}\right)$. Evaluation points for the other two cost functions can be evaluated anywhere within the training domain, which can be useful for study areas that are data limited [59].

2.2.2 Bayesian Neural Networks

Standard feedforward neural networks are parameterized by the weights and biases between each hidden layer. Training these parameters via stochastic gradient descent will result in a single set of optimal parameter values for the above loss functions, which will correspondingly lead to a single set of predictions for given input coordinates. For the hybrid physical modeling framework discussed here, the efficacy of the basal drag neural network depends in large part on the appropriateness of the assumed momentum balance, ice rheological model, etc. Any uncertainties in these assumptions will propagate to uncertainties in the modeled basal drag. Proper quantification of these uncertainties is hence critical for subsequent interpretation of the inferred basal drag.

Here, we utilize Bayesian neural networks with probabilistic loss functions to learn a distribution over the neural network weights for the basal drag network (see Materials and Methods). The weight posterior distribution allows us to generate a distribution of basal drag predictions and derived statistical properties (e.g., mean and sample covariance). Spatial patterns of basal drag covariance can provide important insight into uncertainties within the data and any modeling assumptions. One type of uncertainty can stem from errors in the ice rheology (the exponent n and the flow rate parameter A that influence the dynamic viscosity, as discussed in Materials and Methods) that are propagated through the momentum balance when computing basal drag.

2.3 1D Spatially Varying Drag

To evaluate the neural network representation of basal drag, we first generate 1D SSA simulations for two different cases of frictional parameter distributions (Figure 2). In the first case, we prescribe a constant exponent of $m = 3$ and a spatially varying prefactor, c_b, with values that slowly increase with upstream distance to approximate increasing basal drag. In the second case, we prescribe periodic exponent values with values ranging from approximately 1 to 6, which spans the regimes from linear to approximately plastic sliding. Additionally, we assign values of c_b such that the modeled basal drag is approximately equal to the drag from the first case. In this way, both cases will have similar values of basal drag throughout the simulation but different time-dependent sliding, providing a good test for the recovery of the true frictional parameters from time-dependent observations. For both simulations, we force the system through periodic variations of the longitudinal stress at the terminus to simulate periodic ocean tides. The resulting velocity time series show strong periodicity in time while the ice thicknesses are roughly constant throughout the simulation (Figure S1).

For training the networks $g_{\boldsymbol{\phi}}$ (predicting surface velocity and ice thickness) and $f_{\boldsymbol{\theta}}$ (predicting basal drag), we select a spatial subset spanning the minimum terminus position and 50 km upstream of that position to use as training data for the neural networks $g_{\boldsymbol{\phi}}$ and $f_{\boldsymbol{\theta}}$. This subset includes the portions of the glacier with measurable periodic velocity fluctuations. In principle, one could use the entire simulation domain to reconstruct the full basal drag profile, but we take a subset since we expect recovery of sliding law behavior to be poorly constrained at low velocity variations. To simulate for measurement noise, we add white noise with a standard deviation of 0.5 m/year and Gaussian correlated noise with a lengthscale of 5 km (equivalent to approximately 10 ice thicknesses) and an amplitude of 2 m/yr (approximately 5$\%$ of the mean velocity variation, consistent with observations) to the velocity data [52, 45]. Generally, the correlated noise will have a much larger effect on the inferred basal drag since coherent velocity gradients will be mapped to spurious basal drag variations. Similarly, we add white noise with an amplitude of 0.5 m and correlated noise with the same lengthscale and an amplitude of 2 meters to the ice thickness data, which is equivalent to perfect knowledge of the bed and observation noise of high-quality digital elevation models [48]. While models of bed topography using mass conservation techniques are more accurate for fast-flowing glaciers [49], we still expect errors on the order of several tens of meters which would likely require the addition of an extra topographic variable to $g_{\boldsymbol{\phi}}$ to allow for approximation of uncertain bed topography (as is done for our analysis on Rutford Ice Stream). For the simulated cases here, we assume perfect knowledge of the bed in order to isolate the effects of velocity and surface errors on inferred drag.

After training $g_{\boldsymbol{\phi}}$ and $f_{\boldsymbol{\theta}}$, we can query $f_{\boldsymbol{\theta}}$ for various values of u, x, and t in order to reconstruct the full time history of the basal drag at any point along the simulation domain used during training. In this manner, we can visually examine the τ_b vs. u relationship to infer the underlying physical relationship without needing a closed-form symbolic expression of that relationship. A natural domain for viewing τ_b vs. u is in log space where, for the power-law form of the sliding law, the slope corresponds to $1/m$ and the intercept corresponds to $\log{(c_b)}$. For the forcing environment simulated here (longitudinal stress perturbations applied at the terminus), the sliding parameters are expected to be time-invariant and can be estimated for each point along the glacier. Additionally, since we use Bayesian neural networks for the basal drag, we can generate stochastic predictions of τ_b for any triplet of (u, x, t) in order to compute the mean and standard deviation of the $1/m$ and c_b estimates. As a comparison, we also compute basal drag directly from the noisy surface observations using Equation 7 where we apply a spatial smoothing window of approximately 5 ice thicknesses to the data prior to computation.

For both simulation cases, we are able to accurately recover the true sliding law parameters for the region of the glacier with sufficiently large velocity variations (within ≈40 km of the terminus; Figure 3). As the upstream distance increases, the amplitudes of the velocity fluctuations caused by the stress perturbations applied at the terminus attenuate. Correspondingly, the stochastic predictions for τ_b become more scattered, which ultimately results in increasing uncertainties in both $1/m$ and c_b as the linear fits in log space become more ill-conditioned. Another factor influencing uncertainties is proximity to the edges of the training domain. Here, spatial gradients are not as well constrained as the interior, which will affect computation of the expected basal drag $\tilde{\tau}_b$. Therefore, in practice, it is advisable to extend the training domain to slightly outside the area of interest in order to properly constrain spatial gradients. In a few places along the profile, we observe larger deviations from the true parameter values where higher noise amplitudes affect drag predictions. However, these regions are also associated with larger parameter uncertainties. This association is likely due to the KL-divergence loss in the probabilistic formulation (see Materials and Methods) which provides a spatial smoothing effect by encouraging predictions with low variance. Higher prediction uncertainties are then required to maximize the data likelihood for the locations where the spatially-correlated noise is commensurate with the amplitude of the velocity variations.

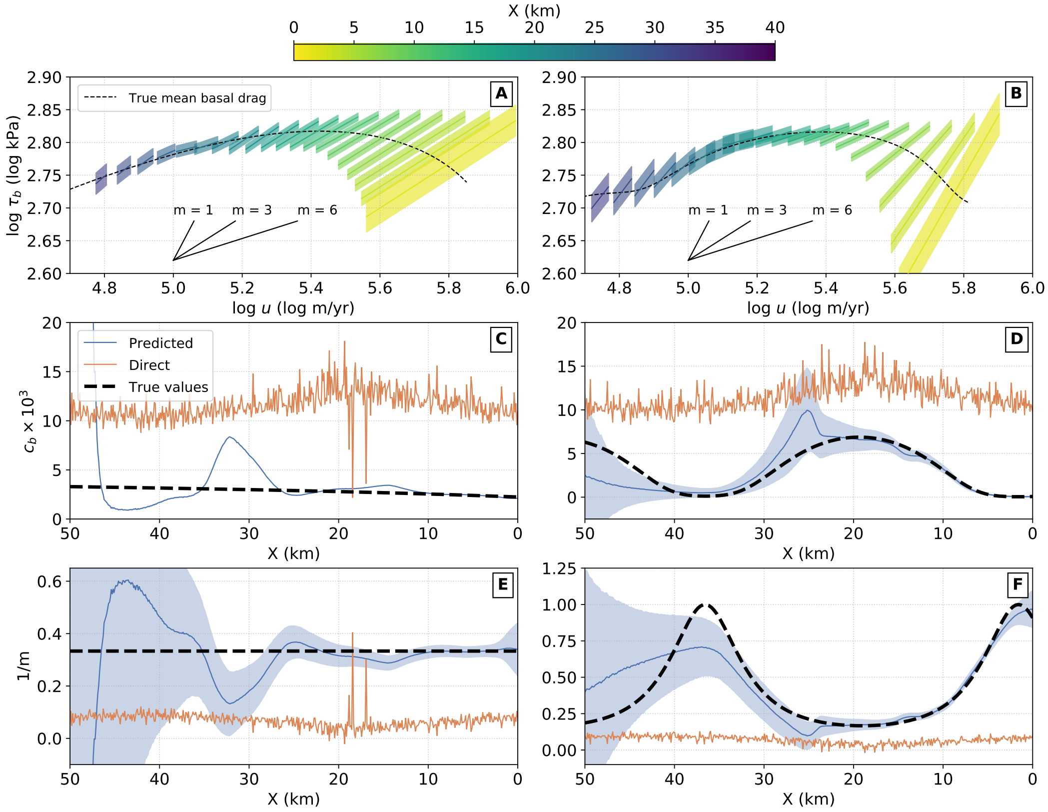

Figure 3: Inferred basal parameter profiles and predicted time-dependent basal drag τ_b vs. sliding velocity u for 1D simulations. Left column corresponds to results for the simulations with spatially-varying prefactor (case I) while the right column correspond to results for simulations with spatially-varying prefactor and exponent (case II). A) Log-domain plot of basal drag vs. sliding velocity for case I. Colors indicate distance upstream of the terminus, where dark lines correspond to a linear fit of stochastic samples and shaded regions correspond to sample standard deviation (3σ). Thin black dashed line indicates true mean basal drag over simulation period, and solid black lines at the bottom illustrate theoretical slopes for $m = 1$, 3, and 6. B) Same as (A) but for case II. C) and (E) Profiles of estimated prefactor, c_b, and exponent, $1/m$, respectively, for case I. Blue lines correspond to the neural network predictions while blue shaded areas are the prediction uncertainties (3σ). Red lines correspond to direct estimates of basal drag using momentum balance of surface observations. Thick black dashed lines correspond to the true values. D) and F) same as (C) and (E) for case II. Sliding law parameter inference is best constrained where velocity variations are high and areas away from edges of training domain.

Another key result is that estimates of basal drag using direct application of Equation 7 lead to highly biased and noisy sliding law parameter estimates, even when significant spatial smoothing is applied to the data prior to application of the momentum balance (Figures 3C-F). The ability of the neural network framework to accurately recover the true parameter values (to the extent where velocity variations are large enough) indicates similar levels of robustness to noise as traditional inverse modeling schemes that apply some form of regularization on the modeled basal drag. Overall, these results show that the neural network framework functions as a time-dependent inversion scheme for the basal drag where common regularization strategies can be implemented analogously through the learning objective [16]. The ability to quantify uncertainties in predictions of basal drag is an important additional benefit of the Bayesian neural network formulation that does not change the complexity of implementation relative to standard neural networks. These uncertainties can be crucial in determining the overall resolving capacity of surface observations in determining the dominant sliding modes.

2.4 1D Time Varying Drag

In the previous section, the sliding law parameters were simulated to be time-invariant. However, for some glaciers and ice streams, basal drag has been hypothesized to evolve in time, e.g. in response to changes in the subglacial hydrological system. As water flows into and out of the hydrological system, the basal water pressure compensates some of the overburden pressure and thus changes the effective pressure (the difference between overburden and water pressures) at the bed. The overall change in effective pressure will thus affect the magnitude of the basal drag and the corresponding flow of ice [29, 73, 26, 15, 71, 47, 78]. Here, we implement a simplified model for temporally varying water pressure by representing the prefactor in the power-law sliding law as a Mohr-Coulomb yield criteria such that

$$c_b\left(x,t\right) = \mu\left(\rho_i g h\left(x,t\right) - p_w\left(x,t\right)\right), \tag{12}$$

where μ is a constant friction coefficient, and the function $p_w\left(x,t\right)$ represents spatially and temporally varying basal water pressure. We model the basal pressure as a periodic pressure wave that propagates upstream in the following manner:

$$p_w\left(x,t\right) = \bar{p}_w + \hat{p}_w e^{-x/L} \cos\left(-\omega t + \frac{\omega}{\mathrm{v}_p} x\right), \tag{13}$$

where $\bar{p}_w$ is a constant water pressure, $\hat{p}_w$ is the amplitude of the pressure oscillations, L is a decay lengthscale (allowing for upstream exponential decay of the pressure perturbation), ω is the angular frequency of the oscillation, and v_p is the wave speed (phase velocity) controlling the upstream propagation speed of the pressure wave. This functional form for the pressure wave approximates diffusive models for subglacial hydrology [71] where the phase velocity and decay lengthscale of the pressure wave is controlled by the conductivity of the hydraulic system. Using the same ice geometry as the previous two 1D simulations, we set values of $\mu = 2 \times 10^{-3}$, $\bar{p}_w = 1000$ kPa, $\hat{p}_w = 500$ kPa, $L = 45$ km, $\omega = 1$ rad/year, and $\mathrm{v}_p = 0.27$ km/day. Furthermore, to investigate the dynamics of a plastically-deforming bed subject to hydrological variations, we generate simulations for $m = 3$ and 10, where the latter approximates a plastic bed. In order to maintain a similar velocity range for the two sliding exponents, we increase the friction coefficient for $m = 10$ to $\mu = 5 \times 10^{-3}$ (in order to match the secular velocities for the $m = 3$ outputs) and reduce the pressure wave amplitude to $\hat{p}_w = 200$ kPa since a plastic bed will result in large velocity variations for a given stress perturbation. The resulting velocity fields for both simulations show similar annual variations as the simulations forced by periodic variations at the terminus (Figure 4A, B). While the velocity variation amplitudes are similar at the terminus for $m = 3$ and 10, the upstream extent of the variations is larger for the latter case, even with a substantially reduced pressure wave amplitude.

Using the same training procedure for $g_{\boldsymbol{\phi}}$ and $f_{\boldsymbol{\theta}}$ as the previous two cases (but without noise added to the data in order to highlight the mechanical effects of the pressure wave), we reconstruct the full time history of the modeled basal drag. The stochastic predictions for $\hat{\tau}_b$ demonstrate that, similar to the previous experiments, drag variations are well constrained in the regions where velocity variations are higher (Figure 4C,D). Generally, decreases in drag are associated with increases in velocity since the propagating pressure wave is the primary driver of speedups in ice flow. However, this trend changes with upstream distance as the pressure wave amplitude decays and longitudinal stress perturbations become the dominant forcing mechanism. The crossover point at which longitudinal stresses become more important is controlled by the pressure wave decay lengthscale, phase velocity, and sliding law

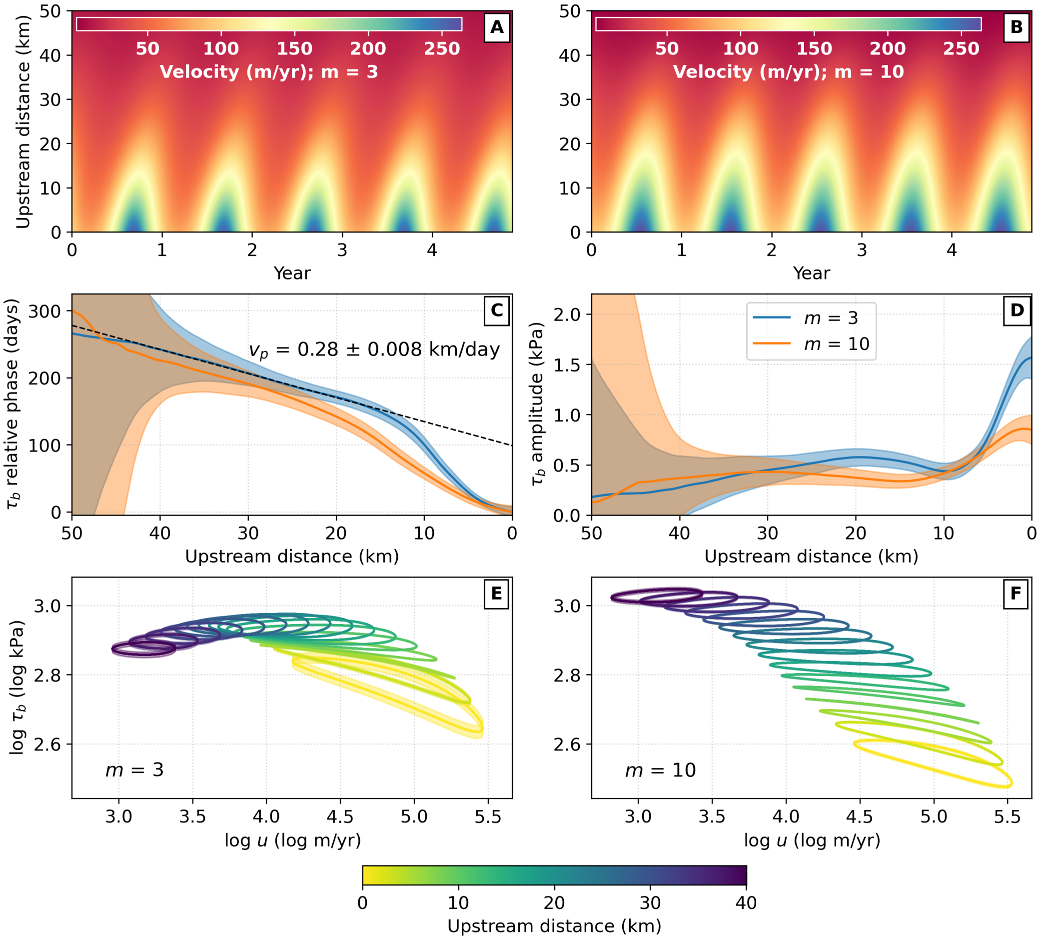

Figure 4: Neural network velocity and basal drag predictions for temporally varying drag simulation. Simulations were conducted with spatially-uniform sliding law exponent values of $m = 3$ and $m = 10$. A) and (B) show spacetime evolution of predicted velocity for $m = 3$ and $m = 10$, respectively. C) Profiles of estimated basal drag periodic phase delay where blue and orange lines correspond to $m = 3$ and $m = 10$, respectively. D) Profiles of estimated basal drag periodic amplitude. E) Log drag. vs. log velocity for select points for $m = 3$ where color indicates distance upstream from the grounding line. Solid lines correspond to mean drag predictions while shaded regions correspond to 3σ uncertainties. F) Same as (E) but for $m = 10$. The amplitude and phase delay profiles combined with the ellipticity of log τ_b vs. log u can be used to infer the propagating pressure wave.

exponent. To illustrate this point further, we fit a temporal function consisting of a linear trend and an annual sinusoid to the $\hat{\tau}_b$ time series at each point while accounting for the uncertainties in $\hat{\tau}_b$. The amplitude and phase delay of the sinusoids, as well as their formal uncertainties, can then be estimated along the glacier (Figure 4C,D). For $m = 3$, we observe a significant phase offset between the first 10 km upstream of the terminus and the rest of the ice stream; this phase offset is minimized for $m = 10$. For the sinusoidal amplitudes, recall that the imposed water pressure variations for $m = 3$ were 2.5x larger than those for $m = 10$. However, the recovered maximum drag amplitude is only twice as large for $m = 3$ compared to $m = 10$, which indicates a negative feedback between the reduction in drag from the pressure wave and an increase in drag resulting from the induced speedup [71]. This negative feedback also manifests as a sharper drop-off in amplitude with upstream distance for $m = 3$. The amplitude reaches a local minimum at the same location where the drag phase gradients are at their peak. For $m = 10$, as with the phase gradients, the amplitude drop-off is much less pronounced.

Another important difference in these pressure wave-driven simulations is that the relationship between τ_b vs. u in the log domain exhibits a cycle (Figure 4E, F), with elliptical behavior arising from varying levels of phase lag between the periodic velocity and basal drag signals (Figure S2). The varying phase lag is again a consequence of competing basal drag perturbations from the pressure wave and balancing of longitudinal stress perturbations resulting from the initial speedup where the latter generally propagates upstream with a higher phase velocity.

The similarity in the velocity variations between the pressure wave-forced simulations in this section and the terminus-forced simulations in the previous section obscures the stark differences in the basal drag evolution between the two model classes. While the neural network-based drag reconstruction is well-constrained for both cases, attribution of the dominant forcing mechanism for a given glacier without *a priori* information is considerably more uncertain. Nevertheless, the strong inverse proportionality between $\hat{\tau}_b$ and u in Figure 4E,F for regions closer to the terminus does suggest that glaciers and ice streams exhibiting similar cycles are likely influenced by time-varying effective pressure. Considering that effective pressure changes can be subsumed into a time-varying sliding law prefactor, simultaneous recovery of both the sliding law prefactor and exponent as shown in the previous section is not possible for glaciers influenced by substantial subglacial hydrological effects. In these cases, independent observations of basal water pressure variations (and thus, prefactor variations) would be needed to recover values of the exponent. Conversely, if *a priori* information about the exponent were available (e.g., the bed is well-approximated by plastic deformation), then it is possible to derive estimates of basal water pressure variations from the time-varying drag [47].

2.5 Rutford Ice Stream, Antarctica

Rutford Ice Stream (RIS) in West Antarctica is a fast-flowing ice stream which flows into the Filchner-Ronne Ice Shelf (Figure 5A). RIS is laterally confined with an average width of approximately 23 km, and most of the forward velocity is due to basal sliding [33, 18, 76]. The high width-to-thickness and slip ratios support the use of the SSA approximations for examining basal drag variations at intermediate to long spatial wavelengths [19, 11]. Furthermore, RIS exhibits strong variations in flow velocity due to tidal forcing where non-zero variations are measured almost 100 km away from the grounding line. While variations in vertical velocity are mostly modulated by diurnal and semi-diurnal tides, along-flow variations are observed primarily at the fortnightly M_{sf} (14.77 day) period [20, 53, 45], which indicates a non-linear response of RIS flow to tidal forcing [22, 71, 69]. While several recent studies have compared different mechanisms for originating along-flow variations at the M_{sf} frequency on the ice shelf [68, 70], our focus in this study is on using the response of ice flow in the grounded ice stream to infer the mechanics of slip at the ice-bed interface. Thus, our analysis focuses on regions of the ice stream greater than 10 km upstream of the grounding line in order to avoid elastic effects due to bending stresses, which are not incorporated into the SSA approximations [69]. We emphasize that a rigorous exploration of the ice stream stress response (including the elastic response) to tidal forcing is outside the scope of this work. Rather, our aim is demonstrate the machine learning-based techniques for inferring time-dependent basal drag on high-quality surface observations.

2.5.1 Data and learning objectives

We use existing data sets to constrain the surface velocity fields and ice-stream geometry. The 3D surface velocity fields were derived from 9 months of synthetic aperture radar (SAR) data collected from multiple viewing angles in order to constrain a parametric surface displacement model consisting of sinusoids corresponding to the primary tidal constituents and a steady-state velocity [45]. Since our main focus is on the along-flow velocity variations (where variations at diurnal and semi-diurnal constituents are minimal [53]), we use only the steady-state velocity and sinusoid periods at the M_{sf} frequency. Geometric information (surface elevation and ice thickness) were obtained from BedMachine V1 [50]. While our analysis is focused on the regions of the ice stream greater than 10 km upstream of the grounding line, our training domain spans from 150 km upstream of the grounding line to regions of the ice shelf within 45 km downstream of the grounding line. With this extended domain, we can confidently constrain the spatial gradients of the observation variables. Additionally, inclusion of the ice shelf also provides a means to validate the rheological parameters since basal drag is expected to be negligible on the shelf (seawater offers very little resistance to ice flow). Here, we use a characteristic temperature of -10° C to calculate an effective depth averaged value of A from tabulated values [10] and a stress exponent $n = 3$ to compute ice viscosity (Materials and Methods), which results in minimal steady-state drag values on the ice shelf.

We use one neural network, g_ϕ, to predict the time-varying velocity components and time-invariant ice thickness and surface elevation. At the fortnightly timescales, ice thickness and driving stress are assumed to be constant in time. By adding the surface elevation variable to the outputs of g_ϕ (as opposed to adding a known bed elevation to the thickness predictions as was done with the simulated data), we implicitly account for uncertainties in the bed topography by treating $s = h + b$ as an additional noisy observation. For the velocity components, rather than outputting the velocity values at any given input $(\mathbf{x}, t)$, we instead output the spatially-varying coefficients of a periodic temporal model (independently for the u and v components), e.g.:

$$u(\mathbf{x}, t) = a(\mathbf{x}) \cos(\omega_{sf} t) + b(\mathbf{x}) \sin(\omega_{sf} t) + u_0(\mathbf{x}), \tag{14}$$

where $\omega_{sf} = 2\pi / T_{sf}$ is the fortnightly angular frequency for the M_{sf} tidal constituent (T_{sf} = 14.77 days), and the coefficients $[a, b, u_0]$ vary in space only. This approach reduces the dimensionality of the neural network inputs to two spatial coordinates while providing physical constraints on the temporal form of the predictions.

We adopt a similar temporal functional form for the outputs of the basal drag network, $f_{\boldsymbol{\theta}}$, where the weights $\boldsymbol{\theta}$ are again trained with probabilistic loss functions. The values of the expected drag, $\tilde{\tau}_b$, are now computed from the 2D SSA equations (Equations 1a, 1b), which only requires an additional input and output dimension for g_ϕ. We assume an ice density ρ_i = 917 kg/m^3. For the basal drag network, $f_{\boldsymbol{\theta}}$, we add another input dimension but restrict the network to predict basal drag magnitude, which simplifies implementation of physics-based loss functions for $\mathcal{L}_{ph}$ and improves physical-consistency of drag predictions (see Supplementary S1 for an example application to 2D simulated data generated with realistic modeling uncertainties). Values for the hyperparameter controlling spatial smoothness of basal drag were chosen using a standard L-curve (Figure S5).

2.5.2 Secular Velocity and Basal Drag Predictions

The predicted along-flow steady-state velocity magnitudes for RIS are in good agreement with the observed velocities (Figure 5B), while the velocity amplitude and phase are also in good agreement with prior studies [45]. The steady-state basal drag magnitudes show a region of very low basal drag from approximately 10–50 km upstream of the grounded line, transitioning to higher drag over short distances (Figure 5G). This transition from a weak to a stronger bed has been inferred in several prior studies [33, 57] and has been associated with a transition from dilatant to stiff sediment [76]. Since RIS is close to steady-state [21], drag variations are mostly in balance with the driving stress (Figure 5E). The drag magnitudes in our training area peak at around 100 km upstream of the grounding line, which is colocated with a local high in the basal topography (Figure S6). Previous numerical studies of RIS have shown that basal topography is the dominant control on surface undulations, which in turn implies that basal topography is the dominant control on secular drag variations at the spatial scale of tens of kilometers [57, 11]. Under the functional form of Equation 12 where μ represents the internal friction coefficient for till, these results support the view that variations in the friction coefficient μ are at much longer wavelengths ($>$ 20 ice thicknesses), with the exception of the low basal drag region. By further assuming a plastic bed with a uniform value of $\mu = 0.5$ (median of

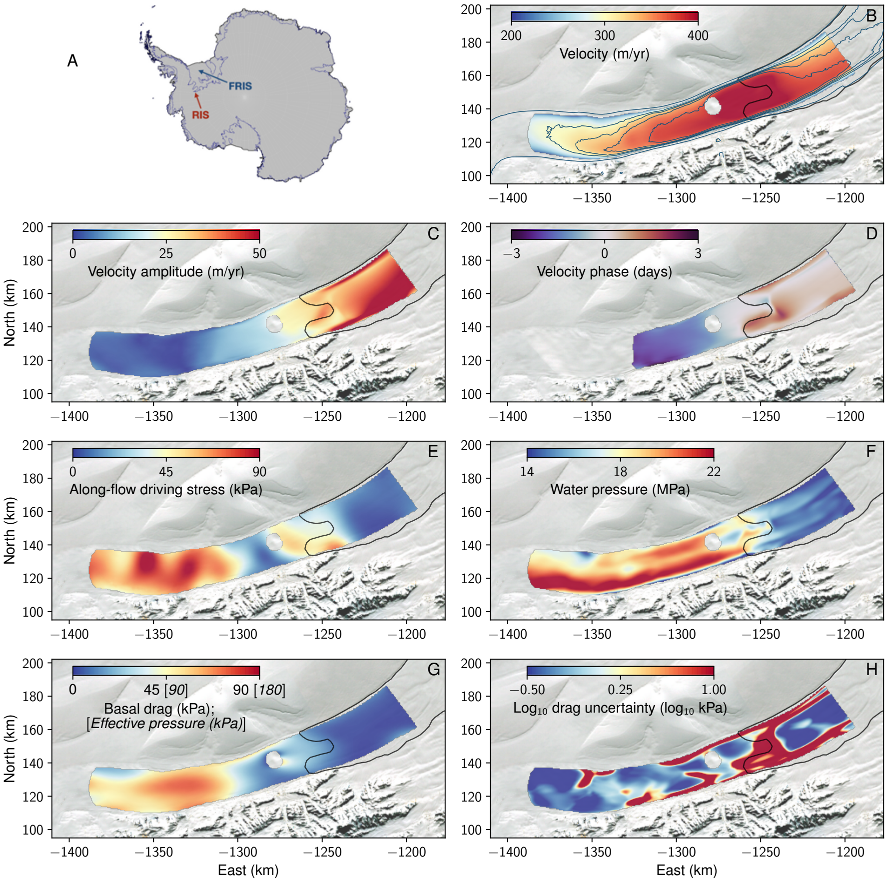

Figure 5: Rutford Ice Stream (RIS) study area and secular surface velocity and basal drag. (A) RIS (red arrow) feeds into the Filchner-Ronne Ice Shelf (FRIS, blue arrow) in West Antarctica. (B) The neural-network-predicted secular velocity magnitude, which is in good agreement with the observed secular velocities from [45] (blue contours at levels of 0, 295, 320, 345, and 370 m/year). The predicted amplitude (C) and phase (D) of the time-dependent velocity variations are also in good agreement with [45] (areas of high phase uncertainty, due to low amplitude variations, masked out). The driving stress (E) is mostly balanced by the neural-network-predicted basal drag (G). By assuming a plastic bed with yield stress determined by the Mohr-Coulomb yield criteria (Eq. 12), effective pressure equals basal drag divided by the internal friction coefficient, $\mu = 0.5$ (pressure values shown in square brackets and italics in (G)). Secular water pressure (F) may then be derived from the effective pressure. Scalar uncertainties for predicted basal drag (H) are generally high in areas with relatively rapid changes in bed slope, such as the margins and near the grounding line (uncertainty values saturate at 10 kPa).

published values [30]), the effective pressure is simply twice the basal drag (Figure 5E), and we can obtain a testable estimate of basal water pressure at RIS by subtracting the effective pressure from the overburden stress (Figure 5F). We explore the implications of bed plasticity on water pressure changes in a later discussion. Finally, uncertainties for the predicted drag are generally highest at the margins and areas with high bed slopes where data gradients are large and work against the Laplacian smoothing penalty (Figure 5H). The zone of large uncertainty in the vicinity of the grounding line is thus also likely driven by a combination of large changes in bed slope and uncertainties in those slopes. Quantification of drag and grounding line migration in these areas has proven challenging and will only improve once more high-quality bed topography data are acquired [70].

2.5.3 Time-dependent Velocity and Basal Drag Predictions

By quantifying the change in velocity and basal drag at different times within the M_{sf} tidal period, we observe significant basal drag variations propagating upstream with values spanning 4 – 6 kPa over the course of the tidal period (Figure 6). Perhaps the most interesting observation is that the upstream propagation of positive velocity variations is associated with a propagating *decrease* in basal drag, which suggests some form of a pressure wave driven by subglacial hydrology (analogous to Figure 4). During the initial speedup of the ice stream, the associated basal drag decreases only slightly, which may signify destructive interference of basal drag reduction and longitudinal stress perturbations originating from loss of buttressing stresses downstream [68, 70]. We reiterate that the inferred basal drag near the grounding line is likely inaccurate since we do not incorporate elasticity of the ice into our stress calculations and bed slopes there are subject to larger uncertainties. However, later in the tidal cycle when velocity speedups have propagated to about 70 km upstream of the grounding line, the basal drag decrease has also propagated upstream while becoming more widespread within the ice stream (Figure 6E,F). We do observe a phase lag between the velocity and drag variations which can be confirmed by the elliptical relationship between τ_b vs. u (Figure 7), a characteristic we previously observed for the 1D simulated pressure waves. The exceptions to this behavior are near the grounding line and in the weaker bed where drag variations are minimal compared to the velocity variations. At greater upstream distances, we can observe a gradual transition in the ellipse orientation, signifying a transition to a stress regime where longitudinal stresses become the primary driver of the velocity variations.

3 Discussion

The availability of time-dependent surface observations of velocity and elevation permit direct estimation of time-varying basal drag satisfying the global stress balance. Coupled with a machine learning model for reconstructing the spatiotemporal function for basal drag, we can retrieve important sliding parameters under certain stress and loading conditions. We discuss the robustness and implications of these results below.

3.1 Inference of Sliding Law Parameters

Under the condition that ice surface velocity variations are driven by processes other than changes in drag at the bed – such as longitudinal stress perturbations at the terminus or grounding line, as may be expected in some cases for seasonal calving cycles, ocean tide effects via hydrostatic stress differences, or changes in buttressing stresses from ice shelves – then, for a general power-law formulation of the sliding law, it is possible to recover both the prefactor and exponent from a linear fit of time-dependent sliding velocity and basal drag predictions in the log domain. Parameter estimation for recently proposed augmented sliding laws that combine the power-law sliding relationship at lower velocities and a rate-independent (plastic) relationship at higher velocities [32, 85, 46] can be accomplished in a similar manner through a nonlinear optimization in the log domain. Verification and refinement of such a law from remote sensing data sets would make significant progress towards unification of laboratory, observational, and theoretical approaches towards understanding glacier sliding dynamics.

For all proposed sliding law functional forms, if the sliding law parameters are known to be time-invariant (but may be spatially-varying), then simultaneous parameter recovery is possible. In cases where the parameters may vary in time, such as when changes in the prefactor are driven by subglacial hydrological processes, then simultaneous recovery is not possible, and one would need additional information about the physical properties of the bed, such as water pressure variations or bed plasticity (which is equivalent to knowing the value of the exponent in the power-law form of the sliding law, as discussed in the following section).

Under applicable conditions, successful recovery of sliding law parameters is largely dependent on the availability and temporal sampling of time-dependent velocity fields. Static velocity snapshots allow only for the estimation of the magnitude of basal drag. Inference of one of the sliding law parameters would require some assumption on the value of the others, as well as an assumption on the form of the sliding law. Time-dependent velocity fields allow for quantification of time-dependent basal drag, permitting joint estimation of all sliding law parameters by quantifying the relationship between drag and sliding velocity at different points within the spatial domain. Furthermore, the

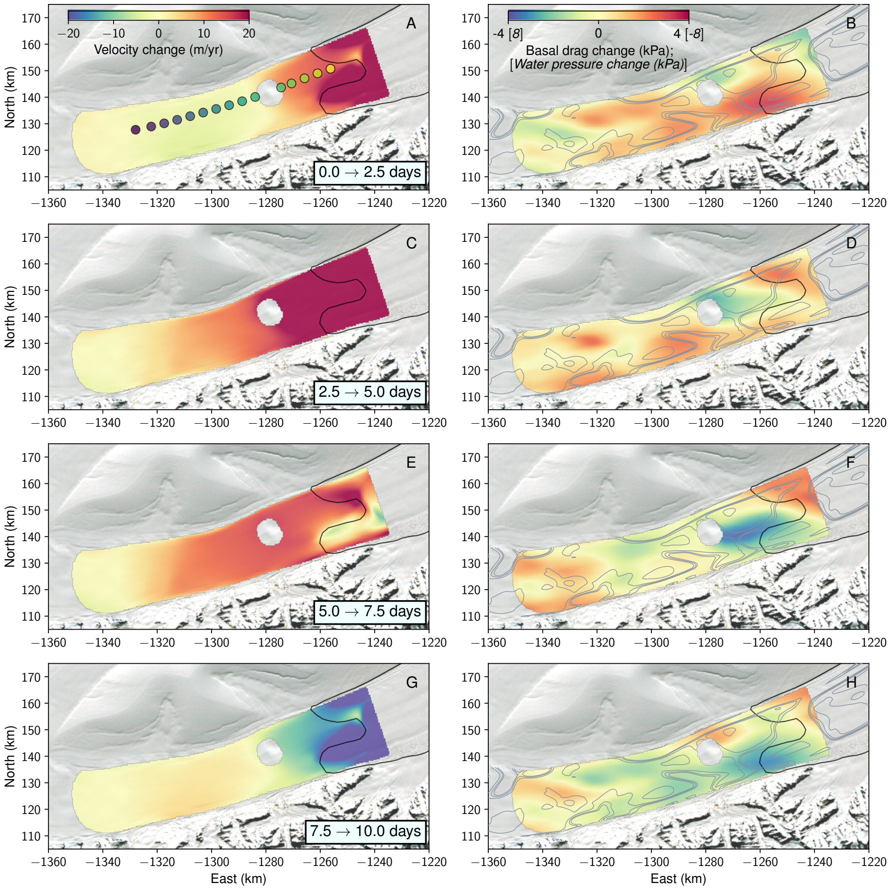

Figure 6: Time-dependent velocity and basal drag magnitude variations for Rutford Ice Stream, Antarctica. Velocity and basal drag variations are shown in the left and right columns, respectively. By assuming a plastic bed, basal water pressure variations can be inferred by scaling drag variations by the internal friction coefficient $\mu = 0.5$ (values indicated in square brackets and italics in (B)). Beginning at a reference time that approximately corresponds to the beginning of the M_{sf} cycle (minimum velocity near the grounding line), velocity and drag variations are measured in 2.5-day intervals: (A, B) 0 – 2.5 days; (C, D) 2.5 – 5 days; (E, F) 5 – 7.5 days; and (G, H) 7.5 – 10 days. Markers in (A) indicate points extracted for Figure 7. Grey contours for right-column plots correspond to the log secular basal drag uncertainties in Figure 5H in intervals of 0.5. In general, an upstream-propagating increase in velocity is associated with an upstream-propagating decrease in basal drag, which suggests that a pressure wave in the subglacial till is responsible for the observed variations in surface velocity.

larger the amplitude of velocity variability at any given location (e.g., amplitude of periodic variations due to ocean tides or seasonal effects), the better constrained the parameters (Figure 3, for example). For study areas where velocity and elevation measurements are more sparse or exhibit higher noise levels, the methods presented here would greatly benefit from a time series preprocessing stage that can fit some smoothly varying time function to the available data to inject stronger *a priori* knowledge about the underlying flow variations [45, 64], as was done for the RIS velocity data.

In this work, surface observations are used to compute the global stress balance directly via momentum balance equations under the assumptions that the rheology of the ice is reasonably well constrained and surface velocities are approximately equal to basal sliding velocities. However, the viscous nature of ice flow acts as a low-pass filter on basal stress variations such that variations with spatial scales < 1 ice thickness can result in similar surface velocities and elevations [24]. Therefore, inversion techniques using finite element models and noisy surface observations generally use regularization schemes to promote smoother basal stress fields [39, 24, 75]. Theoretically, noise-free surface velocity

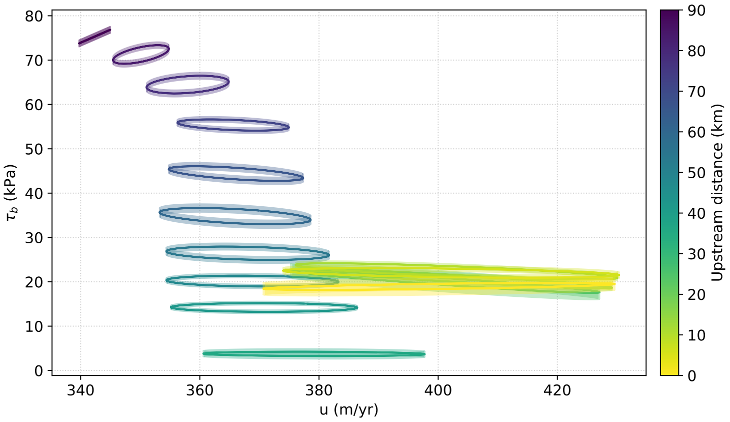

Figure 7: Time series of basal drag vs. velocity for select points along a centerline. Points are colored by distance upstream of the grounding line with locations shown in Figure 6A. Shaded regions indicate 1σ uncertainties in predicted drag.

observations with spatial resolution less than the wavelength of basal stress variability can be used to reconstruct the true basal drag (as demonstrated in this work). Moreover, it has been shown that the transfer function amplitude between variability in basal stress and surface velocities decreases with decreasing spatial wavelengths, but higher slip ratios (ratio of sliding to deformation velocity) can increase the transfer function amplitude [19]. Overall, our method should be most applicable to fast-flowing glaciers which are dominated by basal sliding and where the spatial scale of basal stress variability is greater than the intrinsic resolution of the velocity fields [77].

3.2 Joint Estimation of Basal Drag and Ice Rheology

In this work, we assumed a uniform ice rheology for computing the stress divergence terms of the momentum balance in Equations 1a and 1b. Any underlying variations in the rheology will lead to variations in the inferred basal drag via spatial gradients of the effective dynamic viscosity. When these gradients are small, as would be expected in the central trunk of the glacier, errors in the inferred drag should also be correspondingly small. While uncertainties in the rheology may be partially modeled as uncertainties in the basal drag (Supplementary S1), it may also possible to jointly estimate rheological parameters and drag when certain conditioning and regularizing factors can be applied. As an example, a third neural network can be trained to predict a spatially-varying flow rate parameter, $A(x, y)$, under a different set of physical constraints, e.g. softer ice in high strain-rate areas (such as lateral shear margins) and anisotropic smoothing to enforce lower spatial gradients in the along-flow direction. As demonstrated by [60], such constraints can effectively reduce the inherent trade-offs between rheology and drag variations.

3.3 Rutford Ice Stream and Subglacial Hydrology

In general, speedups in ice flow respond to changes in driving, longitudinal, and basal stresses. A localized perturbation in longitudinal or driving stress (e.g., as a result of a calving event for a tidewater glacier) will result in a non-local redistribution of longitudinal stresses and velocity variations well away from the original perturbation. Similarly, a localized perturbation in basal drag will result in non-local redistribution of longitudinal stresses and velocity changes upstream [32]. On the other end of the spectrum, subglacial hydrological variations that result in traveling "pressure waves" are governed primarily by the properties of the hydraulic network, although indirect effects could arise from changes in surface slope [25, 44]. In this case, surface velocity will respond to a combination of local reductions in basal drag (corresponding to the pressure wave front) and non-local variations in longitudinal stress. Consequently, quantifying velocity variation magnitudes without examining spatial gradients (i.e., strain rate variations) will not distinguish between these different forcing mechanisms, and an analysis of the stress states of the glacier is required [69].

While a comprehensive comparison of the stress response to the different forcing mechanisms is reserved for future work, a simplified analysis of the evolution of longitudinal normal stresses can be used to infer the sign of the corresponding change in basal drag (Section S2). For RIS, gradients of longitudinal normal stresses decrease (become more negative) in response to increases in surface velocity. Therefore, assuming that lateral shear stress also becomes more resistive for increases in velocity, then it follows that a decrease in basal drag is driving the velocity increases upstream. This simplified analysis, which is not subject to any modeling assumptions other than bulk ice rheology, further supports the inferred pressure wave.

Several recent modeling studies have proposed sub-glacial hydrology as the primary driver of long-period along-flow velocity variations near the grounding zone for RIS [70, 82], as well as the high velocity variation amplitudes further upstream [71]. From the perspective of the work presented here, we implicitly assume that the basal drag is varying only at the M_{sf} frequency when we enforce the periodic time representation. This assumption is likely to be valid for the upstream portions of RIS (greater than a few ice thicknesses from the grounding zone) where elastic stress variations have decayed, thus limiting the response of ice flow to viscous effects [80, 71]. Simultaneous tracking of the velocity and basal drag variations suggests that the possible pressure wave lags behind the traveling wave of surface velocity (Figures 6 and 7), which is consistent with a pressure wave speed below the speed of longitudinal stress transmission. This constraint is almost certainly valid for real-world glaciers since pressure-driven subglacial water flow will be resisted by drag in the hydraulic network, so even for highly connected distributed systems, longitudinal stresses will propagate faster than basal drag variations [82].

As previously discussed, estimation of the underlying sliding law parameters from surface observations is not possible without additional information if the parameters vary in time. However, we may still consider different endmembers for the sliding law exponents to explore the implications of the basal water pressure variations. Let us again consider the case where the bed is perfectly plastic such that the secular basal drag is equal to the yield stress, τ_y, of the bed. In this case, drag variations are entirely determined by the Mohr-Coulomb yield criteria in Equation 12. By assuming that ice thickness is approximately constant over (fortnightly) tidal timescales, then it follows that variations in drag take the form $\Delta\tau_b = \mu\Delta p_w$, so that drag is proportional to changes in basal water pressure. For an estimated basal drag variation amplitude of 4 – 5 kPa roughly 20 km upstream of the grounding line, the corresponding water pressure variation would then be 8 – 10 kPa for internal friction coefficient $\mu = 0.5$ (Figure 6). Following the subglacial hydrological model of [71], which assumes subglacial hydrology at RIS can be described as a homogenous porous medium, changes in water pressure can be related to changes in hydrologic head. At the grounding line where the hydrological system is in direct contact with the ocean, hydrologic head is equal to the ocean elevation, and basal water pressure variations can be computed as:

$$\Delta p_w = \rho_w g \Delta S, \tag{15}$$

where ρ_w is the density of seawater and S is the height of the ocean surface. From tidal models and GPS records, tidal amplitudes are approximately 3 meters at RIS [71, 45, 55], which would lead to water pressure amplitudes of approximately 30 kPa at the grounding line. Thus, our estimate of 10 kPa basal water pressure change at a distance of 20 km upstream indicates an e-folding distance of approximately 20 km. Note that doubling the basal water pressure change to 20 kPa is equivalent to an e-folding distance of approximately 50 km, which is the same value for the velocity amplitudes [45]. The amplitudes of basal drag variations estimated for RIS are likely on the lower end of plausible values due to our higher choice for the smoothing hyperparameter (Figure S5), which was necessary to handle uncertainties in the surface and bed topographies. Thus, it is reasonable to expect that estimates of basal water pressure variations are as high as 15 – 20 kPa.

The upstream diffusion of hydrological head variations is a function of the conductivity of the hydrological system and the temporal frequency of the tidal forcing. While estimation of head variations over the grounded ice is beyond the scope of the work, the relative consistency between the estimated basal water pressure variations assuming a plastic bed and those predicted from a simple subglacial hydrological model provides some support for the possibility that the bed of RIS deforms plastically. If the sliding exponent was instead closer to $m = 3$, the negative feedback between of the increased basal drag resistance caused by the velocity speedup would necessitate a nearly factor of two larger water pressure variation (e.g., Figure 4), which would be on the higher end of plausible values. Therefore, independent measurements of time-dependent basal water pressures would likely provide substantial information for constraining the sliding law exponent for RIS.

3.4 Hybrid Physical Modeling and Physics-Informed Neural Networks

Although the use of neural networks for solving ordinary and partial differential equations was introduced over two decades ago [38], only recently have they been widely adopted due to powerful deep learning frameworks and increased compute capabilities [58, 59, 84]. In particular, physics-informed neural networks (PINNs) have proven to be a powerful and flexible approach for predicting outputs of a physical system where data may be limited but the governing equations are known with reasonably high confidence [59]. PINNs work by training a single neural network on a joint loss function of data misfit and physics consistency (e.g., satisfaction of known PDEs). In the terminology of this work, we would train only g_ϕ to reconstruct the velocity and thickness data while ensuring that the expected basal drag (the term in parentheses in Equation 6) satisfied some set of physical and smoothness constraints. By introducing f_θ for predicting basal drag separately, we essentially approximate the distribution of basal drag values with a neural network representation. The primary benefit to this approach is computational due to the nested gradients used for calculating stresses and Laplacian smoothing penalties, which may require up to four nested automatic differentiation calls if smoothness is imposed on drag predictions computed from g_ϕ outputs. Thus, enforcing physical constraints on f_θ improves computational efficiency over the standard PINN approach while affording more flexibility on the types of constraints that can be used. In this work, we demonstrated how smoothness constraints combined with Bayesian regularization of network weights improved prediction of basal drag in the presence of data noise and uncertainties in rheology, analogous to regularization in inverse methods for basal drag (e.g., Figure 3). The additional computational complexity required for optimizing the additional weights for f_θ is significantly less than imposing the full suite of physical constraints on the network weights for g_ϕ.

An alternative learning approach to the hybrid physical modeling discussed here is to learn the dynamics of the entire glacier system. Essentially, a neural network could be trained to predict the time evolution of ice velocity and thickness completely from velocity and thickness time series without utilizing physical information from the momentum balance equations [58]. In this way, the representation of the glacier dynamics would be purely generic and could be learned with minimal supervision, i.e. "end-to-end" learning. However, the main challenge for this approach is generalizability. In order for a pure neural network model to robustly predict the time evolution of a glacier or ice stream *not* seen during training, one would have to train the network with many different simulations spanning the expected parameter sets of all glaciers and ice streams over the globe. In other words, as the distribution of desired testing examples becomes wider, the distribution of training examples would also have to become wider to ensure that predictions are done in an interpolatory manner rather than an extrapolatory one. Considering the wide variety of bed topographies, sliding conditions, ice shelf conditions, climatic environment, and ice geometries, the training data would need to be prohibitively large in order to ensure generalizability without using any prior physics information. One potentially promising area of research utilizes flexible relational inductive biases encoded in graphs for improving generalizability of neural networks [3]. This type of learning would relax the usage of a specific set of momentum balance equations while still utilizing additional information known from physical interactions between velocity and thickness.

3.5 Uncertainty Quantification

Bayesian neural networks allowed for straightforward uncertainty quantification of basal drag predictions where uncertainties are driven by a combination of data noise and ice flow modeling uncertainties. The drag uncertainties could then be propagated to downstream inference of specific sliding law parameters. While the variational Bayesian techniques used here significantly reduced the computational demand for inferring the posterior distributions of the network weights and biases, the use of a mean-field Gaussian approximation for the surrogate posteriors likely results in underestimation of uncertainties when modeling errors are present (Supplementary S1). These limitations may be rectified by using a more complicated error model in the likelihood distribution [14]. From a broader perspective, we believe that the probabilistic learning framework takes a significant step towards general quantification of both data and modeling uncertainties within a geophysical context while lowering the burden to run computationally expensive MCMC methods. This uncertainty quantification for hybrid physical and machine learning models has proven to be useful in related fields such as atmospheric dynamics [79]. Other probabilistic machine learning models, such as Gaussian processes [61], may also be a suitable surrogate for the basal drag, although joint training of neural networks for the surface observation and a Gaussian process for the basal stress would be less straightforward.

Looking to the future, rapid quantification of uncertainties can aid in the development of targeted data acquisition plans. Regions that show large uncertainties in basal drag predictions are likely under-observed either spatially or temporally due to poorly constrained hypersurfaces learned by the neural networks. Therefore, we envision a future data acquisition scenario where neural network models for observed velocity and elevation fields and inferred basal shear stress fields are updated in an online manner, and the corresponding uncertainty fields dictate what datasets would most likely improve the predictions of those models.

4 Conclusion

We have presented a hybrid machine learning framework for learning the time-evolution of basal mechanics for glaciers and ice streams. This approach integrates into the learning procedure well-known ice flow momentum balance equations at various approximation levels. The *a priori* physical knowledge allows for the transformation of ice velocity and thickness/elevation measurements into a domain where a neural network can directly predict basal drag. Furthermore, we demonstrated the utility of variational Bayesian inference for quantifying uncertainties for the basal drag predictions, which will prove to be invaluable for subsequent interpretation of the drag, inference of sliding law parameters, and development of future data acquisition plans. As a real-world example, application of these techniques to time-dependent velocity data over Rutford Ice Stream, Antarctica, resulted in observational evidence of subglacial hydrological effects during the tidal cycle.

From a broader perspective, this work demonstrates a new and rapidly advancing approach for combining the physical knowledge gained from decades of theoretical and experimental work with modern data-driven techniques in order to address an outstanding problem in glacier dynamics, mainly determination of the sliding mode via the form of the inferred sliding law. Under certain forcing environments, we demonstrated that estimation of the value and uncertainty of the exponent in the power-law form of the sliding law is possible with these methods. The exponentially increasing data volume over the fastest flowing areas in the cryosphere demands techniques that combine data efficiency, modeling flexibility, and robustness in the presence of noise, data gaps, and modeling uncertainties. The methods presented here take an important step towards those requirements and present a path forward for future data assimilation tasks for a multitude of disparate data sources.

Appendix A Ice Flow Model

A.1 Governing Equations

In its most general form, glacier flow can be described as an incompressible Stokes flow:

$$\nabla \cdot \boldsymbol{\sigma} + \rho_i \mathbf{g} = \mathbf{0}, \tag{16}$$

$$\mathrm{Tr}\left(\dot{\boldsymbol{\epsilon}}\right) = 0, \tag{17}$$

where $\nabla \cdot \boldsymbol{\sigma}$ is the divergence of the Cauchy stress tensor, $\boldsymbol{\sigma}$, ρ_i is the density of ice, $\mathbf{g}$ is the gravitational acceleration, $\dot{\boldsymbol{\epsilon}}$ is the strain rate tensor, and Tr is the trace operator (here, bold font indicates tensor and vector quantities while regular font represents scalars). Equation 16 describes the stress balance (also referred to as the momentum balance) while Equation 17 represents the incompressibility of ice. The strain rate tensor describes the rate of deformation of ice and is calculated as the symmetric component of the velocity gradient:

$$\dot{\boldsymbol{\epsilon}} = \frac{1}{2}\left(\nabla \mathbf{u} + (\nabla \mathbf{u})^T\right), \tag{18}$$

where $\mathbf{u} = [u, v, w]$ is the velocity vector. To relate the stress tensor components in Equation 16 to velocity components, the constitutive law for incompressible viscous fluids is used:

$$\boldsymbol{\tau} = 2\eta\dot{\boldsymbol{\epsilon}}, \tag{19}$$

where $\boldsymbol{\tau} = \boldsymbol{\sigma} + p\mathbf{I}$ is the deviatoric stress tensor, $p = \mathrm{Tr}(\boldsymbol{\sigma})/3$ is the isotropic pressure, and $\mathbf{I}$ is the identity matrix. The non-Newtonian effective ice dynamic viscosity, η, is given as:

$$\eta = \frac{1}{2} A^{-\frac{1}{n}} \dot{\epsilon}_e^{\frac{1-n}{n}}, \tag{20}$$

where n is the stress exponent in Glen's flow law, $\dot{\epsilon}_e$ is the effective strain rate (square root of the second invariant of the strain rate tensor), and A is the flow rate factor which depends on properties of the ice (e.g., temperature, interstitial liquid water content, crystal size/orientation, and impurity content). In practice, many studies have found that various approximations to the computationally-expensive full Stokes equations (Equations 16-17) are able to reconstruct observed velocity fields fairly well for certain glacier geometries and result in similar implied glacier mechanics. For the types of glaciers and ice streams we examine in this study, the Shallow Ice Shelf/Stream Approximation (SSA) [41] is most commonly used and assumes: i) ice thickness is much smaller than the horizontal span; ii) most of the forward motion of glaciers is due to sliding at the bed (i.e., vertical shearing is negligible); and iii) total vertical normal stress is equal to the ice overburden pressure. Under these assumptions, the 3D momentum balance can be depth averaged along the z-dimension, and by using the constitutive law in Equation 19, the approximate 2D momentum balance is expressed as (identical to the main text):

$$\frac{\partial}{\partial x}\left(2\eta h\left(2\frac{\partial u}{\partial x}+\frac{\partial v}{\partial y}\right)\right)+\frac{\partial}{\partial y}\left(\eta h\left(\frac{\partial u}{\partial y}+\frac{\partial v}{\partial x}\right)\right)-\tau_{bx}=\rho_i g h\frac{\partial s}{\partial x}, \tag{21a}$$

$$\frac{\partial}{\partial y}\left(2\eta h\left(2\frac{\partial v}{\partial y}+\frac{\partial u}{\partial x}\right)\right)+\frac{\partial}{\partial x}\left(\eta h\left(\frac{\partial u}{\partial y}+\frac{\partial v}{\partial x}\right)\right)-\tau_{by}=\rho_i g h\frac{\partial s}{\partial y}, \tag{21b}$$

where h is the ice thickness, τ_{bx} and τ_{by} represent the x- and y-components of basal shear stress, and s is the ice surface elevation. The vertical velocity component w can be recovered using the incompressibility condition. The above momentum balance states that the gravitational horizontal driving stresses of ice flow (terms on the right-hand side) are balanced by a combination of horizontal gradients of deviatoric stresses and drag at the base of the glacier, τ_b.

A.2 1D Shallow Ice Stream Model Boundary Conditions

Following previous work on 1D flowline models, we enforce two Neumann boundary conditions at the edges of the spatial domain [81, 54]. At the ice divide boundary condition ($x = 0$), a symmetric ice sheet is assumed such that $\partial u/\partial x = 0$. At the grounding line (assuming no ice shelf), the boundary condition is derived from the difference between the hydrostatic pressure of water and ice:

$$\frac{\partial u}{\partial x}=f_s A\left[\frac{1}{4}\rho_i g h\left(1-\frac{\rho_i}{\rho_w}\right)\right]^n, \tag{22}$$

where ρ_w is the density of ocean water and f_s is a scalar factor used to apply a time-varying force on the calving face [54]. While Equation 22 is not strictly applicable to marine-terminating ice streams with no ice shelf, it provides a convenient way to apply longitudinal stress perturbations originating at the terminus. Thus, we can generate time-dependent ice velocity and thickness fields representative of those observed at tidewater glaciers that respond to changes in regional oceanic and climate conditions. For all 1D simulations, we use a flow rate factor $A = 1.2 \times 10^{-24}\mathrm{s}^{-1}\mathrm{Pa}^{-3}$, which corresponds to a temperature of -5° C and an exponent $n = 3$ [10]. We solve these equations in a staggered fashion by solving for u in Equation 3 under the stated boundary conditions for a given thickness profile, h, using Newton's method. Mass continuity gives the time evolution of ice thickness, h:

$$\frac{\partial h}{\partial t}=a-\frac{\partial q}{\partial x}, \tag{23}$$

where a is the surface mass balance (difference between snow accumulation and ablation) and $q = hu$ is the width-averaged ice flux. Thus, we implement a forward Euler step for Equation 23 to update the thickness profile.

Appendix B Neural Network Architecture and Training

We use feedforward networks for all neural networks in this work. The hidden layers have the form $\mathbf{W}\mathbf{x}+\mathbf{b}$ followed by an activation with a hyperbolic tangent (tanh) function. During our experiments, we found that activation functions that were continuously differentiable (e.g., tanh or exponential rectified linear units (ELU)) resulted in smoother spatial gradients of output variables than the rectified linear unit (ReLU). We found very little difference in training convergence speed between tanh and ELU activations. The outputs of all networks are linear (i.e., no activation is applied).

Neural networks tasked with reconstructing velocity and thickness observations were prescribed 4-6 hidden layers where each hidden layer consisted of 50 or 100 hidden units. The exact architectures varied for each problem and were qualitatively chosen based on a balance between reconstruction accuracy, spatial smoothness of the reconstruction, and computational efficiency. Regardless, the tradeoffs between the metrics were minor, and the data reconstructions for all network architectures were largely consistent. The neural networks for basal drag predictions were prescribed 4 hidden layers where each hidden layer consisted of 50 units. In this way, we effectively applied more regularization for these networks as compared with the data networks since our prior assumption for the spatial distribution of basal shear stress is one that is smooth.

B.1 Bayesian Neural Networks

In this work, we quantify uncertainties within our hybrid model using Bayesian neural networks [12, 43]. These networks place probability distributions over the weights and biases, which results in probability distributions for predictions rather than a single value. Without loss of generality, let us consider a single-layer neural network model (perceptron) with inputs $\mathbf{x}$, outputs $\mathbf{d}$, and a tanh activation function:

$$\mathbf{d} = \tanh\left(\mathbf{W}\mathbf{x}\right) + \mathcal{N}\left(\mathbf{0}, \boldsymbol{\sigma}\right), \tag{24}$$

where $\mathcal{N}\left(\mathbf{0}, \boldsymbol{\sigma}\right)$ represents zero-mean, normally-distributed errors scaled by the standard deviation $\boldsymbol{\sigma}$ (for notational brevity, we have omitted the bias vector $\mathbf{b}$ in this discussion). The *likelihood* of observing the data $\mathbf{d}$ given certain values for $\mathbf{W}$ can be described by the distribution $p(\mathbf{d}|\mathbf{W})$. Then, using Bayes' theorem:

$$p\left(\mathbf{W}|\mathbf{d}\right) \propto p(\mathbf{d}|\mathbf{W})p\left(\mathbf{W}\right), \tag{25}$$

where the posterior distribution $p\left(\mathbf{W}|\mathbf{d}\right)$ describes the probability of the values of $\mathbf{W}$ after observing the data, and $p\left(\mathbf{W}\right)$ are the prior probabilities for $\mathbf{W}$. This formulation allows us to encode our prior beliefs on the range of values for the layer weights, as well as the uncertainty structure of the data.

Samples from the posterior distribution $p\left(\mathbf{W}|\mathbf{d}\right)$ can be drawn using Markov Chain Monte Carlo (MCMC) techniques, but for large neural networks with many layers, the computational cost becomes prohibitive [6]. Alternatively, one can use variational Bayesian methods which have proven to be computationally efficient for deep learning models [37, 63]. These methods make use of a *surrogate* posterior distribution to approximate the true posterior distribution, e.g. $q_{\boldsymbol{\lambda}}\left(\mathbf{W}|\mathbf{d}\right) \approx p\left(\mathbf{W}|\mathbf{d}\right)$. The form of the surrogate distribution $q_{\boldsymbol{\lambda}}\left(\mathbf{W}|\mathbf{d}\right)$ is specified beforehand and is parameterized by $\boldsymbol{\lambda}$, e.g. the mean and standard deviation of a normal distribution. The learning objective becomes finding the optimal values for $\boldsymbol{\lambda}$ such that $q_{\boldsymbol{\lambda}}\left(\mathbf{W}|\mathbf{d}\right)$ best approximates the true posterior $p\left(\mathbf{W}|\mathbf{d}\right)$. Mathematically, the variational learning objective is expressed as a minimization of the Kullback-Leibler (KL) divergence between the surrogate posterior and the true posterior:

$$\boldsymbol{\lambda} = \arg\min_{\boldsymbol{\lambda}} D_{KL}\left(q_{\boldsymbol{\lambda}}\left(\mathbf{W}|\mathbf{d}^k\right) \| p\left(\mathbf{W}|\mathbf{d}\right)\right). \tag{26}$$

It can be shown that minimization of the KL-divergence is equivalent to maximization of the Evidence Lower Bound (ELBO) [6]:

$$\mathcal{L}\left(\boldsymbol{\lambda}; \mathbf{d}^k\right) = \mathbb{E}_{q_{\boldsymbol{\lambda}}\left(\mathbf{W}|\mathbf{d}^k\right)}\left[\log p\left(\mathbf{d}^k|\mathbf{W}\right)\right] - \beta D_{KL}\left(q_{\boldsymbol{\lambda}}\left(\mathbf{W}|\mathbf{d}^k\right) \| p\left(\mathbf{W}\right)\right). \tag{27}$$

The first term in the ELBO corresponds to expectation of the data log-likelihood for the k-th data example while the second term measures the KL-divergence between the surrogate posterior and the prior. This second term acts as a form of regularization on the estimated weights of the neural network and can help prevent overfitting. Additionally, we multiply the KL-divergence by a scalar β in order to weight the relative contribution of the regularization effect on the ELBO [27].

In this work, we use the TensorFlow Probability package [13] to train a Bayesian neural network for the basal drag function. We use normal distributions for the prior probabilities for the weights and biases (zero mean with unit variance). The surrogate posterior distributions are assigned to be independent normal distributions, i.e. the network weights are assumed to be independent of each other. This approach, referred to as a mean-field variational approximation, can often result in underestimation of uncertainties when compared to using full MCMC. Finally, we use a normal distribution for the likelihood function, but we parameterize the standard deviation of the likelihood, σ, as a learnable parameter to (partially) represent the situation where we expect modeling errors, i.e. *epistemic* uncertainty.

B.2 Training

Weight matrices for all networks are initialized from a normal distribution with variances specified by $s = 1/\sqrt{a}$ where a is the number of input hidden units for each layer. Inputs to all networks are normalized to be zero-mean with unit variance. We use the Adam optimizer [36] with a learning rate of 0.0002 and train for 500–1000 epochs (each epoch is defined as a complete pass through the training data). Finally, we use a train/test split where 85% of the data is used for training and the remaining 15% is used for validation.

We use the Python API for TensorFlow [1] and TensorFlow Probability [13] for neural network construction and training.

Acknowledgments

Funding for this work was provided by the Earl A Killian III (1978) and Waidy Lee Fund and the NEC Corporation Fund for Research in Computers and Communications. Computing resources were partially funded through a Microsoft AI For Earth computing grant. **Author contributions:** B.R. conceived of the presented idea, implemented the ice flow simulations and deep learning methods, and wrote the manuscript with support from B.M. B.M. also provided interpretation of the results. T.B. helped develop the physics-informed deep learning methods. **Competing interests:** The authors declare that they have no competing interests. **Data and materials availability:** All simulation data and deep learning training code will be made publicly available on https://github.com/bryanvriel/LearningBasalMechanics pending scientific review. Derived velocity components for Rutford Ice Stream, Antarctica are available from the authors upon request. Original COSMO-SkyMed products (copyright ASI Agenzia Spaziale Italiana, 2013-2016) are archived at Jet Propulsion Laboratory and were processed under license from ASI as part of a collaborative project between CIDOT and JPL/Caltech. Bed topography for Antarctica available at https://nsidc.org/data/NSIDC-0756/versions/1.

Supplementary materials

Supplementary Text
Sec. S1. 2D Shallow Ice Stream Simulations.
Sec. S2. Inference of Basal Drag Variations from Longitudinal Stresses.
Fig. S1. 1D Simulated time-dependent velocity and thickness profiles.
Fig. S2. Illustration of effect of phase lag between two periodic variables.
Fig. S3. Geometry and mean velocity and thickness for 2D ice flow simulations.
Fig. S4. Maps of estimated basal parameters for 2D simulation outputs.
Fig. S5. L-curve for smoothing hyperparameter selection for Rutford Ice Stream.
Fig. S6. Bed elevation for Rutford Ice Stream.
Fig. S7. Residuals between neural network predictions and observations for Rutford Ice Stream.
Fig. S8. Profiles of changes in longitudinal stress for different types of forcing.

References

[1] Martín Abadi, Ashish Agarwal, Paul Barham, Eugene Brevdo, Zhifeng Chen, Craig Citro, Greg S. Corrado, Andy Davis, Jeffrey Dean, Matthieu Devin, Sanjay Ghemawat, Ian Goodfellow, Andrew Harp, Geoffrey Irving, Michael Isard, Yangqing Jia, Rafal Jozefowicz, Lukasz Kaiser, Manjunath Kudlur, Josh Levenberg, Dandelion Mané, Rajat Monga, Sherry Moore, Derek Murray, Chris Olah, Mike Schuster, Jonathon Shlens, Benoit Steiner, Ilya Sutskever, Kunal Talwar, Paul Tucker, Vincent Vanhoucke, Vijay Vasudevan, Fernanda Viégas, Oriol Vinyals, Pete Warden, Martin Wattenberg, Martin Wicke, Yuan Yu, and Xiaoqiang Zheng. TensorFlow: Large-scale machine learning on heterogeneous systems, 2015. Software available from tensorflow.org.

[2] Andy Aschwanden, Mark A Fahnestock, Martin Truffer, Douglas J Brinkerhoff, Regine Hock, Constantine Khroulev, Ruth Mottram, and S Abbas Khan. Contribution of the greenland ice sheet to sea level over the next millennium. *Science advances*, 5(6):eaav9396, 2019.

[3] Peter W Battaglia, Jessica B Hamrick, Victor Bapst, Alvaro Sanchez-Gonzalez, Vinicius Zambaldi, Mateusz Malinowski, Andrea Tacchetti, David Raposo, Adam Santoro, Ryan

Faulkner, et al. Relational inductive biases, deep learning, and graph networks. *arXiv preprint arXiv:1806.01261*, 2018.

[4] Atılım Günes Baydin, Barak A Pearlmutter, Alexey Andreyevich Radul, and Jeffrey Mark Siskind. Automatic differentiation in machine learning: a survey. *The Journal of Machine Learning Research*, 18(1):5595–5637, 2017.

[5] Yoshua Bengio, Aaron Courville, and Pascal Vincent. Representation learning: A review and new perspectives. *IEEE transactions on pattern analysis and machine intelligence*, 35(8):1798–1828, 2013.

[6] Christopher M Bishop. *Pattern recognition and machine learning*. springer, 2006.

[7] Helmut Bölcskei, Philipp Grohs, Gitta Kutyniok, and Philipp Petersen. Optimal approximation with sparsely connected deep neural networks. *SIAM Journal on Mathematics of Data Science*, 1(1):8–45, 2019.

[8] Johannes H Bondzio, Mathieu Morlighem, Hélène Seroussi, Thomas Kleiner, Martin Rückamp, Jeremie Mouginot, Twila Moon, Eric Y Larour, and Angelika Humbert. The mechanisms behind jakobshavn isbræ's acceleration and mass loss: A 3-d thermomechanical model study. *Geophysical Research Letters*, 44(12):6252–6260, 2017.

[9] John A Church, Peter U Clark, Anny Cazenave, Jonathan M Gregory, Svetlana Jevrejeva, Anders Levermann, Mark A Merrifield, Glenn A Milne, R Steven Nerem, Patrick D Nunn, et al. Sea level change. Technical report, PM Cambridge University Press, 2013.

[10] Kurt M Cuffey and William Stanley Bryce Paterson. *The Physics of Glaciers*. Academic Press, 2010.

[11] Jan De Rydt, G Hilmar Gudmundsson, HFJ Corr, and Poul Christoffersen. Surface undulations of antarctic ice streams tightly controlled by bedrock topography. *Cryosphere*, 7:407–417, 2013.

[12] John S Denker and Yann LeCun. Transforming neural-net output levels to probability distributions. In *Advances in neural information processing systems*, pages 853–859, 1991.

[13] Joshua V. Dillon, Ian Langmore, Dustin Tran, Eugene Brevedo, Srinivas Vasudevan, Dave Moore, Brian Patton, Alex Alemia, Matt Hoffman, and Rif A. Saurous. Tensorflow Distributions. *arXiv preprint arXiv:1711.10604*, 2017.

[14] Zacharie Duputel, Piyush S Agram, Mark Simons, Sarah E Minson, and James L Beck. Accounting for prediction uncertainty when inferring subsurface fault slip. *Geophysical Journal International*, 197(1):464–482, 2014.

[15] Gwenn E Flowers. Modelling water flow under glaciers and ice sheets. *Proceedings of the Royal Society A: Mathematical, Physical and Engineering Sciences*, 471(2176):20140907, 2015.

[16] F. Gillet-Chaulet. Assimilation of surface observations in a transient marine ice sheet model using an ensemble kalman filter. *The Cryosphere*, 14(3):811–832, 2020.

[17] F Gillet-Chaulet, G Durand, O Gagliardini, C Mosbeux, J Mouginot, F Rémy, and C Ritz. Assimilation of surface velocities acquired between 1996 and 2010 to constrain the form of the basal friction law under Pine Island Glacier. *Geophysical Research Letters*, 43(19):10–311, 2016.

[18] G. H. Gudmundsson. Tides and the flow of Rutford Ice Stream, West Antarctica. *Journal of Geophysical Research: Earth Surface*, 112(F4), 2007.

[19] G Hilmar Gudmundsson. Transmission of basal variability to a glacier surface. *Journal of Geophysical Research: Solid Earth*, 108(B5), 2003.

[20] G Hilmar Gudmundsson. Fortnightly variations in the flow velocity of rutford ice stream, west antarctica. *Nature*, 444(7122):1063–1064, 2006.

[21] GH Gudmundsson and Adrian Jenkins. Ice-flow velocities on Rutford Ice Stream, West Antarctica, are stable over decadal timescales. *Journal of Glaciology*, 55(190):339–344, 2009.

[22] Hilmar Gudmundsson. Ice-stream response to ocean tides and the form of the basal sliding law. *The Cryosphere*, 5:259–270, 2011.

[23] M Habermann, M Truffer, and D Maxwell. Changing basal conditions during the speed-up of Jakobshavn Isbræ, Greenland. *Cryosphere*, 7(6), 2013.

[24] Marijke Habermann, David Maxwell, and Martin Truffer. Reconstruction of basal properties in ice sheets using iterative inverse methods. *Journal of Glaciology*, 58(210):795–808, 2012.

[25] I. J. Hewitt and A. C. Fowler. Seasonal waves on glaciers. *Hydrological Processes*, 22(19):3919–3930, 2008.

[26] IJ Hewitt. Seasonal changes in ice sheet motion due to melt water lubrication. *Earth and Planetary Science Letters*, 371:16–25, 2013.

[27] Irina Higgins, Loic Matthey, Arka Pal, Christopher Burgess, Xavier Glorot, Matthew Botvinick, Shakir Mohamed, and Alexander Lerchner. beta-vae: Learning basic visual concepts with a constrained variational framework. *Iclr*, 2(5):6, 2017.

[28] I. M. Howat, C. Porter, B. E. Smith, M.-J. Noh, and P. Morin. The reference elevation model of antarctica. *The Cryosphere*, 13(2):665–674, 2019.

[29] Almut Iken and Robert A Bindschadler. Combined measurements of subglacial water pressure and surface velocity of Findelengletscher, Switzerland: conclusions about drainage system and sliding mechanism. *Journal of Glaciology*, 32(110):101–119, 1986.

[30] Neal R Iverson. Shear resistance and continuity of subglacial till: hydrology rules. *Journal of Glaciology*, 56(200):1104–1114, 2010.

[31] I Joughin, B Smith, I Howat, and T Scambos. Measures Greenland ice velocity: selected glacier site velocity maps from InSAR. *NASA National Snow and Ice Data Center Distributed Active Archive Center, Boulder, Colorado, USA*, 2011.

[32] I. Joughin, B. E. Smith, and C. G. Schoof. Regularized Coulomb friction laws for ice sheet sliding: application to Pine Island Glacier, Antarctica. *Geophysical Research Letters*, 46(9):4764–4771, 2019.

[33] Ian Joughin, Jonathan L Bamber, Ted Scambos, Slawek Tulaczyk, Mark Fahnestock, and Douglas R MacAyeal. Integrating satellite observations with modelling: basal shear stress of the Filcher-Ronne ice streams, Antarctica. *Philosophical Transactions of the Royal Society A: Mathematical, Physical and Engineering Sciences*, 364(1844):1795–1814, 2006.

[34] Ian Joughin, Ben E Smith, Ian M Howat, Dana Floricioiu, Richard B Alley, Martin Truffer, and Mark Fahnestock. Seasonal to decadal scale variations in the surface velocity of jakobshavn isbrae, greenland: Observation and model-based analysis. *Journal of Geophysical Research: Earth Surface*, 117(F2), 2012.

[35] Anuj Karpatne, Gowtham Atluri, James H Faghmous, Michael Steinbach, Arindam Banerjee, Auroop Ganguly, Shashi Shekhar, Nagiza Samatova, and Vipin Kumar. Theory-guided data science: A new paradigm for scientific discovery from data. *IEEE Transactions on Knowledge and Data Engineering*, 29(10):2318–2331, 2017.

[36] Diederik P Kingma and Jimmy Ba. Adam: A method for stochastic optimization. *arXiv preprint arXiv:1412.6980*, 2014.

[37] Diederik P Kingma and Max Welling. Auto-encoding variational Bayes. *arXiv preprint arXiv:1312.6114*, 2013.

[38] Isaac E Lagaris, Aristidis Likas, and Dimitrios I Fotiadis. Artificial neural networks for solving ordinary and partial differential equations. *IEEE transactions on neural networks*, 9(5):987–1000, 1998.

[39] E Larour, H Seroussi, M Morlighem, and E Rignot. Continental scale, high order, high spatial resolution, ice sheet modeling using the Ice Sheet System Model (ISSM). *Journal of Geophysical Research: Earth Surface*, 117(F1), 2012.

[40] Yann LeCun, Yoshua Bengio, and Geoffrey Hinton. Deep learning. *nature*, 521(7553):436–444, 2015.

[41] Douglas R MacAyeal. Large-scale ice flow over a viscous basal sediment: Theory and application to ice stream B, Antarctica. *Journal of Geophysical Research: Solid Earth*, 94(B4):4071–4087, 1989.

[42] Douglas R MacAyeal. A tutorial on the use of control methods in ice-sheet modeling. *Journal of Glaciology*, 39(131):91–98, 1993.

[43] David JC MacKay. Bayesian neural networks and density networks. *Nuclear Instruments and Methods in Physics Research Section A: Accelerators, Spectrometers, Detectors and Associated Equipment*, 354(1):73–80, 1995.

[44] BM Minchew and Colin R Meyer. Dilation of subglacial sediment governs incipient surge motion in glaciers with deformable beds. *Proceedings of the Royal Society A*, 476(2238):20200033, 2020.

[45] BM Minchew, M Simons, B Riel, and P Milillo. Tidally induced variations in vertical and horizontal motion on Rutford Ice Stream, West Antarctica, inferred from remotely sensed observations. *Journal of Geophysical Research: Earth Surface*, 122(1):167–190, 2017.

[46] Brent Minchew and Ian Joughin. Toward a universal glacier slip law. *Science*, 368(6486):29–30, 2020.

[47] Brent Minchew, Mark Simons, Helgi Björnsson, Finnur Pálsson, Mathieu Morlighem, Helene Seroussi, Eric Larour, and Scott Hensley. Plastic bed beneath Hofsjökull Ice Cap, central Iceland, and the sensitivity of ice flow to surface meltwater flux. *Journal of Glaciology*, 62(231):147–158, 2016.

[48] Delwyn Moller, Scott Hensley, Jeremie Mouginot, Joshua Willis, Xiaoqing Wu, Christopher Larsen, Eric Rignot, Ronald Muellerschoen, and Ala Khazendar. Validation of glacier topographic acquisitions from an airborne single-pass interferometer. *Sensors*, 19(17):3700, 2019.

[49] M. Morlighem, C. N. Williams, E. Rignot, L. An, J. E. Arndt, J. L. Bamber, G. Catania, N. Chauché, J. A. Dowdeswell, B. Dorschel, I. Fenty, K. Hogan, I. Howat, A. Hubbard, M. Jakobsson, T. M. Jordan, K. K. Kjeldsen, R. Millan, L. Mayer, J. Mouginot, B. P. Y. Noël, C. O'Cofaigh, S. Palmer, S. Rysgaard, H. Seroussi, M. J. Siegert, P. Slabon, F. Straneo, M. R. van den Broeke, Wilhelm Weinrebe, M. Wood, and K. B. Zinglersen. Bedmachine v3: Complete bed topography and ocean bathymetry mapping of Greenland from multibeam echo sounding combined with mass conservation. *Geophysical Research Letters*, 44(21):11051–11061, 2017.

[50] Mathieu Morlighem, Eric Rignot, Tobias Binder, Donald Blankenship, Reinhard Drews, Graeme Eagles, Olaf Eisen, Fausto Ferraccioli, René Forsberg, Peter Fretwell, et al. Deep glacial troughs and stabilizing ridges unveiled beneath the margins of the Antarctic ice sheet. *Nature Geoscience*, 13(2):132–137, 2020.

[51] Mathieu Morlighem, Eric Rignot, Helene Seroussi, Eric Larour, H Ben Dhia, and Denis Aubry. Spatial patterns of basal drag inferred using control methods from a full-stokes and simpler models for pine island glacier, west antarctica. *Geophysical Research Letters*, 37(14), 2010.

[52] J. Mouginot, E. Rignot, and B. Scheuchl. Continent-wide, interferometric SAR phase, mapping of Antarctic ice velocity. *Geophysical Research Letters*, 46(16):9710–9718, 2019.

[53] T Murray, A M Smith, M A King, and G P Weedon. Ice flow modulated by tides at up to annual periods at Rutford Ice Stream, West Antarctica. *Geophysical Research Letters*, 34(18):L18503–6, 2007.

[54] Faezeh M Nick, Andreas Vieli, Ian M Howat, and Ian Joughin. Large-scale changes in Greenland outlet glacier dynamics triggered at the terminus. *Nature Geoscience*, 2(2):110, 2009.

[55] L. Padman, M. R. Siegfried, and H. A. Fricker. Ocean tide influences on the antarctic and greenland ice sheets. *Reviews of Geophysics*, 56(1):142–184, 2018.

[56] Claire Porter, Paul Morin, Ian Howat, Myoung-Jon Noh, Brian Bates, Kenneth Peterman, Scott Keesey, Matthew Schlenk, Judith Gardiner, Karen Tomko, Michael Willis, Cole Kelleher, Michael Cloutier, Eric Husby, Steven Foga, Hitomi Nakamura, Melisa Platson, Jr. Wethington, Michael, Cathleen Williamson, Gregory Bauer, Jeremy Enos, Galen Arnold, William Kramer, Peter Becker, Abhijit Doshi, Cristelle D'Souza, Pat Cummens, Fabien Laurier, and Mikkel Bojesen. ArcticDEM, 2018.

[57] Mélanie Raymond Pralong and G Hilmar Gudmundsson. Bayesian estimation of basal conditions on rutford ice stream, west antarctica, from surface data. *Journal of Glaciology*, 57(202):315–324, 2011.

[58] Maziar Raissi. Deep hidden physics models: Deep learning of nonlinear partial differential equations. *The Journal of Machine Learning Research*, 19(1):932–955, 2018.

[59] Maziar Raissi, Paris Perdikaris, and George E Karniadakis. Physics-informed neural networks: A deep learning framework for solving forward and inverse problems involving nonlinear partial differential equations. *Journal of Computational Physics*, 378:686–707, 2019.

[60] Meghana Ranganathan, Brent Minchew, Colin R. Meyer, and G. Hilmar Gudmundsson. A new approach to inferring basal drag and ice rheology in ice streams, with applications to West Antarctic ice streams. *Journal of Glaciology*, page 1–14, 2020.

[61] Carl Edward Rasmussen. Gaussian processes in machine learning. In *Summer School on Machine Learning*, pages 63–71. Springer, 2003.

[62] Markus Reichstein, Gustau Camps-Valls, Bjorn Stevens, Martin Jung, Joachim Denzler, Nuno Carvalhais, et al. Deep learning and process understanding for data-driven Earth system science. *Nature*, 566(7743):195–204, 2019.

[63] Danilo Jimenez Rezende, Shakir Mohamed, and Daan Wierstra. Stochastic backpropagation and approximate inference in deep generative models. *arXiv preprint arXiv:1401.4082*, 2014.

[64] B. Riel, B. Minchew, and I. Joughin. Observing traveling waves in glaciers with remote sensing: New flexible time series methods and application to Sermeq Kujalleq (Jakobshavn Isbræ), Greenland. *The Cryosphere*, in press:1–32, 2020.

[65] E. Rignot, J. Mouginot, and B. Scheuchl. Ice Flow of the Antarctic Ice Sheet. *Science*, 333(6048):1427–1430, 2011.

[66] Catherine Ritz, Tamsin L Edwards, Gaël Durand, Antony J Payne, Vincent Peyaud, and Richard CA Hindmarsh. Potential sea-level rise from Antarctic ice-sheet instability constrained by observations. *Nature*, 528(7580):115–118, 2015.

[67] Alexander A Robel, Hélène Seroussi, and Gerard H Roe. Marine ice sheet instability amplifies and skews uncertainty in projections of future sea-level rise. *Proceedings of the National Academy of Sciences*, 116(30):14887–14892, 2019.

[68] Alexander A Robel, Victor C Tsai, Brent Minchew, and Mark Simons. Tidal modulation of ice shelf buttressing stresses. *Annals of Glaciology*, 58(74):12–20, 2017.

[69] S H R Rosier and G H Gudmundsson. Tidal controls on the flow of ice streams. *Geophysical Research Letters*, 43(9):4433–4440, 2016.

[70] S. H. R. Rosier and G. H. Gudmundsson. Exploring mechanisms responsible for tidal modulation in flow of the filchner–ronne ice shelf. *The Cryosphere*, 14(1):17–37, 2020.

[71] S H R Rosier, G Hilmar Gudmundsson, and J A M Green. Temporal variations in the flow of a large Antarctic ice-stream controlled by tidally induced changes in the subglacial water system. *The Cryosphere*, 9(4):1649–1661, 2015.

[72] C. Schoof. The effect of cavitation on glacier sliding. *Proceeding of the Royal Society of London. Series A, Mathematical and Physical Sciences*, 461:609–627, 2005.

[73] C. Schoof. Ice-sheet acceleration driven by melt supply variability. *Nature*, 468(7325):803–806, 2010.

[74] Christian Schoof. Marine ice-sheet dynamics. part 1. the case of rapid sliding. *Journal of Fluid Mechanics*, 573:27, 2007.

[75] Daniel R Shapero, Ian R Joughin, Kristin Poinar, Mathieu Morlighem, and Fabien Gillet-Chaulet. Basal resistance for three of the largest Greenland outlet glaciers. *Journal of Geophysical Research: Earth Surface*, 121(1):168–180, 2016.

[76] EC Smith, AM Smith, RS White, AM Brisbourne, and HD Pritchard. Mapping the ice-bed interface characteristics of Rutford Ice Stream, West Antarctica, using microseismicity. *Journal of Geophysical Research: Earth Surface*, 120(9):1881–1894, 2015.

[77] LA Stearns and CJ Van der Veen. Friction at the bed does not control fast glacier flow. *Science*, 361(6399):273–277, 2018.

[78] Laura A Stevens, Ian J Hewitt, Sarah B Das, and Mark D Behn. Relationship between greenland ice sheet surface speed and modeled effective pressure. *Journal of Geophysical Research: Earth Surface*, 123(9):2258–2278, 2018.

[79] Andrew Stuart and Aretha Teckentrup. Posterior consistency for Gaussian process approximations of Bayesian posterior distributions. *Mathematics of Computation*, 87(310):721–753, 2018.

[80] J. Thompson, M. Simons, and V. C. Tsai. Modeling the elastic transmission of tidal stresses to great distances inland in channelized ice streams. *The Cryosphere*, 8(6):2007–2029, 2014.

[81] Andreas Vieli and Antony J Payne. Assessing the ability of numerical ice sheet models to simulate grounding line migration. *Journal of Geophysical Research: Earth Surface*, 110(F1), 2005.

[82] KLP Warburton, DR Hewitt, and JA Neufeld. Tidal grounding-line migration modulated by subglacial hydrology. *Geophysical Research Letters*, page e2020GL089088, 2020.

[83] Johannes Weertman. On the sliding of glaciers. *Journal of glaciology*, 3(21):33–38, 1957.

[84] Yinhao Zhu, Nicholas Zabaras, Phaedon-Stelios Koutsourelakis, and Paris Perdikaris. Physics-constrained deep learning for high-dimensional surrogate modeling and uncertainty quantification without labeled data. *Journal of Computational Physics*, 394:56–81, 2019.

[85] Lucas K. Zoet and Neal R. Iverson. A slip law for glaciers on deformable beds. *Science*, 368(6486):76–78, 2020.